Presynaptic Rac1 controls synaptic strength through the regulation of synaptic vesicle priming

(Abbreviated title): Presynaptic Rac1 regulates synaptic strength

Christian Keine[1,2,3], Mohammed Al-Yaari[1], Tamara Radulovic[1,2,3], Connon I. Thomas[4], Paula Valino Ramos[1], Debbie Guerrero-Given[4], Naomi Kamasawa[4], and Samuel M. Young, Jr.[1,5^].

[1]Department of Anatomy and Cell Biology, University of Iowa, Iowa City, IA, USA
[2]Department of Human Medicine, Carl-von-Ossietzky University Oldenburg, Oldenburg, Germany
[3]Research Center Neurosensory Science, Oldenburg, Germany
[4]Electron Microscopy Core Facility, Max Planck Florida Institute, Jupiter, FL, USA
[5]Department of Otolaryngology, Iowa Neuroscience Institute, University of Iowa, Iowa City, IA, USA.

^Correspondence
Samuel M. Young, Jr. PhD
Department of Anatomy and Cell Biology
University of Iowa
PBDB 5322
169 Newton Road
Iowa City, IA 52242
Email: samuel-m-young@uiowa.edu

ORCIDs:

Christian Keine:	0000-0002-8953-2593
Mohammed Al-Yaari	0000-0003-3196-266X
Tamara Radulovic:	0000-0002-2825-9773
Connon I. Thomas:	0000-0003-0995-9667
Naomi Kamasawa:	0000-0002-8926-5309
Samuel M. Young, Jr.:	0000-0002-7589-7612

Abstract

Synapses contain a limited number of synaptic vesicles (SVs) that can be released in response to action potentials (APs). Therefore, sustaining synaptic transmission over a wide range of AP firing rates and timescales depends on SV release and replenishment. Although actin dynamics impact synaptic transmission, how presynaptic regulators of actin signaling cascades control SV release and replenishment remain unresolved. Rac1, a Rho GTPase, is a regulator of actin signaling cascades that control synaptogenesis, neuronal development, and postsynaptic function. However, the presynaptic role of Rac1 in regulating synaptic transmission is unclear. To unravel the roles of presynaptic Rac1 in controlling synaptic transmission, we performed selective presynaptic ablation of Rac1 at the mature mouse calyx of Held. We show that presynaptic Rac1 deletion leads to increased synaptic strength due to increased SV release probability which results in faster SV replenishment and increased spontaneous SV release rates with no change in presynaptic morphology or active zone ultrastructure. Based on our data, we conclude that presynaptic Rac1 controls synaptic strength by regulating the intrinsic SV release probability through SV priming. Therefore, we propose that presynaptic Rac1 is a key regulator of synaptic transmission and plasticity.

Introduction

Information encoding in the nervous system requires synaptic transmission to drive and sustain action potentials (APs) over rapid and large fluctuations of AP firing rates (Reinagel and Laughlin, 2001; Theunissen and Elie, 2014; Brette, 2015; Azarfar et al., 2018). However, the number of synaptic vesicles (SVs) that can be released in response to an AP, the readily releasable pool (RRP), is limited (Alabi and Tsien, 2012). Therefore, tight regulation of SV release and replenishment is required for synaptic reliability and temporal precision needed to encode information (Neher, 2010; Hallermann and Silver, 2013). Priming is the process that creates fusion-competent SVs and is a key step in the SV life cycle that regulates RRP size, replenishment, and the SV release probability (P_r) (Klug et al., 2012; Neher and Brose, 2018). Furthermore, modulation of the temporal dynamics of priming is highly dependent on presynaptic Ca^{2+} levels. Importantly, human mutations in molecules that regulate priming are associated with neurological disorders (Waites and Garner, 2011; Wondolowski and Dickman, 2013; Torres et al., 2017; Bonnycastle et al., 2021). Therefore, elucidating the molecular mechanisms that regulate priming is critical to understanding the diversity of information encoding in the nervous system.

Actin is a central component of both the presynaptic and postsynaptic compartment with diverse roles in regulating synaptic function and neuronal circuit development. Manipulation of actin dynamics or the presynaptic AZ proteins implicated in regulating actin dynamics affects SV release and replenishment rates, as well as P_r (Morales et al., 2000; Sakaba and Neher, 2003; Cingolani and Goda, 2008; Waites et al., 2011; Lee et al., 2012, 2013; Montesinos et al., 2015; Rust and Maritzen, 2015). However, due to disparate results, the role of presynaptic actin signaling cascades in regulating SV release and replenishment is controversial. Finally, in contrast to the postsynaptic compartment, our understanding of how presynaptic regulators of actin signaling cascades control SV release and replenishment are in the early stages.

Rac1, a Rho GTPase, is a critical regulator of actin signaling cascades (Bosco et al., 2009; Yasuda, 2017), and human mutations in Rac1 are associated with neurological disorders (Bai et al., 2015; Reijnders et al., 2017; Zamboni et al., 2018). Rac1 is involved in multiple processes which control synaptogenesis, axon guidance, neuronal development, and postsynaptic function to regulate neuronal circuit function (Bai et al., 2015). Although Rac1 is expressed in both the pre and postsynaptic compartment (Threadgill et al., 1997; Doussau et al., 2000; Kumanogoh et al., 2001; O'neil et al., 2021), its presynaptic role in regulating synaptic transmission is not well understood. However, recent work using cultured hippocampal neurons proposed that presynaptic Rac1 is a negative regulator of SV replenishment (O'neil et al., 2021), though at which steps in the SV lifecycle it exerts its regulatory role is unknown. Finally, how Rac1 regulates the temporal dynamics of RRP release and replenishment in a native neuronal circuit remains elusive.

To unravel the regulatory roles of presynaptic Rac1 in regulating synaptic transmission, we utilized the calyx of Held, an axosomatic presynaptic terminal in the auditory brainstem, which is the sole input to drive AP spiking in the principal cells of the medial nucleus of the trapezoid body (MNTB) (Borst and Soria Van Hoeve, 2012; Joris and Trussell, 2018). In the calyx of Held, RRP dynamics are tightly regulated to support the early stages of auditory processing, but the properties of SV release and replenishment are similar to conventional presynaptic terminals in the central nervous system (Iwasaki and Takahashi, 1998, 2001; Iwasaki et al., 2000; Taschenberger et al., 2002; Sätzler et al., 2002; Rollenhagen and Lübke, 2006; Neher and Sakaba, 2008; Alabi and Tsien, 2012; Eggermann et al., 2012; Hallermann and Silver, 2013; Kaeser and Regehr, 2014; Schneggenburger and Rosenmund, 2015). In addition, molecular manipulations specific to the calyx of Held can be carried out at different neuronal circuit developmental stages (Wimmer et al., 2006; Young and Neher, 2009; Chen et al., 2013; Lübbert et al., 2019). To elucidate the roles of presynaptic Rac1 in regulating synaptic transmission while avoiding its role in synaptogenesis, axon guidance, and neuronal

development, we selectively deleted Rac1 2 days after hearing onset in postnatal day (P) 14 mouse calyx of Held, which is functionally mature, while neuronal circuit properties are “adult-like” and subsequently determined how the loss of Rac1 impacted calyx of Held/MTNB transmission at the adult stage (P28 onwards) (Sonntag et al., 2009, 2011; Crins et al., 2011). We found that presynaptic Rac1 deletion does not affect the calyx of Held morphology or active zone (AZ) ultrastructure but leads to increased synaptic strength. This increase in synaptic strength is due to increased SV release probability which results in faster SV replenishment and increased spontaneous SV release rates. Additionally, we found that loss of Rac1 leads to an increase in the temporal delay of EPSC onset with an increase in asynchronous release during high-frequency train stimuli. Taken together, our data demonstrate that presynaptic Rac1 is a key molecule that controls synaptic strength through SV priming steps that regulate SV release probability.

Results

Presynaptic deletion of Rac1 after hearing onset does not impact calyx of Held morphology or AZ ultrastructure

Rac1 is found in the presynaptic terminal (Doussau et al., 2000; O'neil et al., 2021) and regulates synaptogenesis, axon guidance, and neuronal development (Xu and Chen, 2019; Zhang et al., 2021). In this study, we aimed to elucidate Rac1's presynaptic function in controlling synaptic transmission and plasticity independent of its role in regulating synapse development and maturation at the calyx of Held/MNTB synapse. To do so, we injected HdAd co-expressing Cre recombinase and EGFP into the cochlear nucleus (CN) of P14 *Rac1*$^{flox/flox}$ animals when the calyx of Held/MNTB synapse is considered "adult-like" and analyzed the calyx of Held/MNTB synapse at P28 onwards (Fig. 1A, Sonntag et al., 2009, 2011; Crins et al., 2011). Since Rac1 acts as a central molecule controlling synapse development and morphology, it was important to determine whether the loss of Rac1 after hearing onset altered the calyx of Held morphology or AZ ultrastructure. Morphology was analyzed from 3D reconstructions of calyx terminals from confocal z-stack images acquired from *Rac1*$^{+/+}$ and *Rac1*$^{-/-}$ animals at P28 and we found no change in calyx surface area or volume (Fig. 1B). To determine if the loss of Rac1 impacted AZ ultrastructure, we performed ultrathin section TEM and analyzed AZ length, SV distribution, and the number of docked SVs and found no difference between *Rac1*$^{+/+}$ and *Rac1*$^{-/-}$ (Fig. 1C). Therefore, we conclude that after hearing onset Rac1 is not essential for regulating calyx of Held morphology and AZ ultrastructure.

Loss of Rac1 increases synaptic strength through an increase in SV release probability.

Perturbations of the presynaptic actin cytoskeleton impact synaptic transmission and plasticity in multiple model systems and synapses (Cole et al., 2000; Sakaba and Neher, 2003; Bleckert et al., 2012; Rust and Maritzen, 2015; Miki et al., 2016; Gentile et al., 2022; Wu and Chan, 2022). Since Rac1 is an actin cytoskeleton regulator, we examined how the loss of Rac1 impacted AP-evoked synaptic transmission and short-term plasticity. Afferent fiber stimulation of calyx axons

was performed using 50 AP at two stimulation frequencies (50 Hz and 500 Hz) representing typical *in vivo* firing rates at the calyx at low or high activity, respectively. AMPAR-mediated ESPCs from MNTB principal cells innervated by transduced (*Rac1*$^{-/-}$) and non-transduced calyces (*Rac1*$^{+/+}$) were recorded in 1.2 mM external Ca^{2+} concentration and 36-37°C to mimic *in vivo* conditions (Fig. 2A, B). Analyzing the first EPSC ($EPSC_1$) of the stimulus train, we found a dramatic increase in EPSC amplitude upon Rac1 deletion (*Rac*$^{+/+}$ = 1.3 ± 0.4 nA vs. *Rac1*$^{-/-}$ = 3 ± 1.1 nA, p=2.5e-5, n=15/15, Fig. 2C) with no change in EPSC waveform. Plotting EPSC amplitudes vs. stimulation number revealed differences in short-term plasticity between *Rac1*$^{+/+}$ and *Rac1*$^{-/-}$. At 50 Hz stimulation, both *Rac1*$^{+/+}$ and *Rac1*$^{-/-}$ showed short-term depression which was emphasized in *Rac1*$^{-/-}$ with increased steady-state depression relative to $EPSC_1$. Despite the stronger relative short-term depression, absolute steady-state EPSC amplitudes were almost two-fold larger in *Rac1*$^{-/-}$ (*Rac1*$^{+/+}$ = 0.47 ± 0.14 nA vs. *Rac1*$^{-/-}$ = 0.84 ± 0.22 nA, p = 4e-5, n = 15/15) and replenishment rates were increased (*Rac1*$^{+/+}$ = 23 ± 7 nAs^{-1} vs. *Rac1*$^{-/-}$ = 42 ± 11 nAs^{-1}, p = 2.4e-5, n = 15/15). At 500 Hz stimulation, *Rac1*$^{+/+}$ showed robust short-term facilitation which was absent in *Rac1*$^{-/-}$ (PPR: $Rac1^{+/+}$ = 1.2 ± 0.1 vs. $Rac1^{-/-}$ = 1 ± 0.1, p = 3.4e-6, n = 15/15). Similar to 50 Hz stimulation, *Rac1*$^{-/-}$ showed increased levels of relative steady-state depression at 500 Hz stimulation. Notably, absolute steady-state EPSC amplitude and replenishment rates at 500 Hz stimulation frequency were not different between *Rac1*$^{+/+}$ and *Rac1*$^{-/-}$.

Since the loss of Rac1 increased synaptic strength and altered short-term plasticity it was important to determine if these changes were caused by an increase in RRP size, SV release probability (P_r), or both. We estimated the RRP size using 500 Hz stimulation frequency since it effectively depletes the RRP for both *Rac1*$^{+/+}$ and *Rac1*$^{-/-}$ and employed three methods to estimate the RRP: EQ, NpRf, and SMN with correction (Elmqvist and Quastel, 1965; Neher, 2015; Thanawala and Regehr, 2016). Both, the EQ and NpRf method reported no change in RRP size, while the SMN method detected a slight RRP increase in *Rac1*$^{-/-}$ calyces.

Subsequently, we calculated the initial P_r by dividing the amplitude of the 1st EPSC by the estimated RRP sizes and all three methods revealed a two-fold increase in P_r (SMN: *Rac1*$^{+/+}$ = 0.09 ± 0.02 vs. *Rac1*$^{-/-}$ = 0.15 ± 0.03, p = 4.8e-7; NpRf: *Rac1*$^{+/+}$ = 0.09 ± 0.02 vs. *Rac1*$^{-/-}$ = 0.17 ± 0.03, p = 2.5e-7; EQ: *Rac1*$^{+/+}$ = 0.08 ± 0.02 vs. *Rac1*$^{-/-}$ = 0.16 ± 0.03, p = 2.4e-7, n = 15/15). Next, we calculated the steady-state P_r (steady-state EPSC divided by the calculated remaining RRP) and found an increase in *Rac1*$^{-/-}$ calyces at both 50 Hz (*Rac1*$^{+/+}$ = 0.09 ± 0.02 vs. *Rac1*$^{-/-}$ = 0.16 ± 0.03, p = 9.4e-7, n=15/15) and 500 Hz stimulation (*Rac1*$^{+/+}$ = 0.09 ± 0.02 vs. *Rac1*$^{-/-}$ = 0.15 ± 0.03, p = 3.2e-7, n = 15/15). These findings show that presynaptic Rac1 deletion increases short-term depression by elevating both initial and steady-state P_r with little or no effect on RRP size. Therefore, we conclude that Rac1 controls synaptic strength as a negative regulator of P_r.

Loss of Rac1 increases mEPSC frequency but not amplitude

The two steps in the SV life cycle that impact RRP size and P_r are molecular priming and positional priming (Neher and Brose, 2018). Molecular priming encompasses the steps that render an SV fusion competent and regulates the intrinsic SV fusogenicity, defined as the fusion willingness of an SV (Basu et al., 2007; Xue et al., 2010; Schotten et al., 2015). Positional priming consists of the steps that place molecularly primed SVs close to the voltage-gated calcium channels (VGCCs) (Neher, 2010). The distance between SV and VGCCs, coupling, is a critical determinant of the speed and efficacy of AP-evoked release (Eggermann et al., 2012). Spontaneous SV release is independent of VGCCs (Schneggenburger and Rosenmund, 2015; Kavalali, 2020) and the frequency of miniature EPSC (mEPSCs) can be used as a readout of changes in SV fusogenicity with increased SV fusogenicity causing higher mEPSC frequencies (Basu et al., 2007; Schotten et al., 2015; Dong et al., 2018). Therefore, to ascertain if the increase in P_r was caused by an increase in intrinsic SV fusogenicity, we recorded mEPSCs from *Rac1*$^{+/+}$ and *Rac1*$^{-/-}$ calyces (Fig. 3) and found a four-fold increase in mEPSC frequency (*Rac1*$^{+/+}$ = 3.4 ± 4.4 Hz vs. *Rac1*$^{-/-}$ = 14.3 ± 6.5 Hz, p = 3.4e-4, n = 15/11) with no change in

mEPSC amplitude or waveform. To rule out that the increased mEPSC frequencies were due to changes in Cav2.1 currents we recorded mEPSCs in the presence of 200 µM Cd^{2+}, a non-specific VGCC blocker. Since the addition of Cd^{2+} did not affect mEPSC frequencies (control = 14.6 ± 3.2 Hz vs. cadmium = 14.9 ± 2 Hz, p = 0.84, n = 3/3), we conclude that Rac1 regulates P_r by controlling intrinsic SV fusogenicity independent of Ca^{2+}.

Loss of Rac1 increases temporal delays in AP evoked release

Although we found an increase in SV fusogenicity, this does not rule out an additional role for Rac1 in regulating positional priming. In the mature calyx of Held, nanodomain release results in a fast onset of synchronous AP-evoked EPSCs to encode auditory information (Fedchyshyn and Wang, 2005). The time between presynaptic AP and EPSC onset (EPSC onset delay) is determined by the distance between SVs and VGCC which defines the time it takes for Ca^{2+} to bind to the Ca^{2+} sensor and trigger SV release (Fedchyshyn and Wang, 2007). Thus, EPSC onset delays can serve as a readout of changes in positional priming, as increases in onset delay would indicate more loosely coupled SVs and vice versa. Therefore, we measured EPSC onset delays during 50 Hz and 500 Hz stimulation (Fig. 4A, B) and found them to become progressively larger during stimulation for both *Rac1*$^{+/+}$ and *Rac1*$^{-/-}$ calyces. At 50 Hz, the increase in EPSC onset delay was comparable between *Rac1*$^{+/+}$ and *Rac1*$^{-/-}$ amounting to about 60 µs between the first and the last ten EPSCs. At 500 Hz stimulation, however, EPSC onset delays increased more rapidly in *Rac1*$^{-/-}$ with steady-state EPSC onsets delays being significantly larger for *Rac1*$^{-/-}$ compared to *Rac1*$^{+/+}$ (*Rac1*$^{+/+}$ = 94± 32 µs vs. *Rac1*$^{-/-}$= 131 ± 29 µs, p = 0.004, n = 15/15).

In addition to EPSC onset delays, the synchronicity of AP-evoked release can be used as an indirect readout of positional priming since synchronous release represents SVs that are tightly coupled and asynchronous release is representative of loosely coupled SVs (Sakaba, 2006; Schneggenburger and Rosenmund, 2015). Furthermore, EPSC synchronicity is independent of conduction delay, the delay between stimulus and the time when the AP reaches

the presynaptic terminal. Therefore, we determined EPSC synchronicity by dividing the EPSC amplitude by the EPSC charge for both 50 Hz and 500 Hz stimulation (Fig. 4C). The synchronicity of the first EPSC was comparable between *Rac1*$^{+/+}$ and *Rac1*$^{-/-}$ while steady-state EPSC synchronicity at 50 Hz was slightly lower in *Rac1*$^{-/-}$ (*Rac1*$^{+/+}$ = 3.2 ± 0.3 nA pC^{-1} vs. Rac1 KO = 2.9 ± 0.2 nA pC^{-1}, p = 0.006). At 500 Hz stimulation, steady-state EPSC synchronicity in *Rac1*$^{-/-}$ calyces was further deteriorated and 20% lower compared to *Rac1*$^{+/+}$ (*Rac1*$^{+/+}$ = 2.4 ± 0.3 nA pC^{-1} vs. *Rac1*$^{-/-}$ = 1.9 ± 0.3 nA pC^{-1}, p = 2.3e-4). These findings indicate that SV release was less synchronous in *Rac1*$^{-/-}$ in a time- and frequency-dependent manner.

Taken together, we found that *Rac1*$^{-/-}$ had longer EPSC onsets and decreased EPSC synchronicity, especially at high stimulation frequencies. Therefore, we conclude that the increase of synaptic strength in *Rac1*$^{-/-}$ calyces is not due to changes in positional priming that result in tighter SV coupling since tighter coupling would lead to shorter EPSC onset delays and higher synchronicity in the *Rac1*$^{-/-}$ calyces.

Loss of Rac1 facilitates EPSC and RRP recovery

Modulation of molecular priming steps regulates RRP recovery (Neher and Brose, 2018; Ritzau-Jost et al., 2018). Since Rac1 deletion increased SV fusogenicity and P_r throughout the stimulus train, we hypothesized that RRP recovery was faster in the absence of Rac1. To test how the loss of Rac1 influences RRP recovery, we carried afferent fiber stimulation using a paired train protocol consisting of a 500 Hz depleting train (50 APs) followed by a second 500 Hz test train at varying recovery intervals (Fig. 5). Recovery was then measured for both single EPSCs and the RRP. For single EPSC recovery, we measured both absolute and fractional recovery by normalizing the $EPSC_1$ amplitude of the test train to the $EPSC_1$ amplitude of the control train relative to steady-state EPSC amplitudes. Recovery of $EPSC_1$ was significantly faster in *Rac1*$^{-/-}$ compared to *Rac1*$^{+/+}$ for both absolute and fractional recovery (absolute: *Rac1*$^{+/+}$ τ_w = 2.4 s vs *Rac1*$^{-/-}$ τ_w = 1.7 s, p = 1e-12; fractional: *Rac1*$^{+/+}$ τ_w = 1.8 s vs *Rac1*$^{-/-}$ τ_w = 1.3 s, p = 3.2e-8, n = 15/15, Fig. 5A). Next, we analyzed fractional RRP recovery by dividing the RRP estimate of

the test train by the RRP estimate of the depleting train and found that RRP recovery rates were about 40% faster in *Rac1*$^{-/-}$ (*Rac1*$^{+/+}$ τ_w = 1.14 s vs *Rac1*$^{-/-}$ τ_w = 0.7 s, p = 1.1e-9, n = 15/15; Fig 5B). Finally, we calculated the paired-pulse ratios ($EPSC_2/EPSC_1$) of the test train to estimate release probability as a function of recovery interval. Independent of recovery interval, PPR was consistently lower in *Rac1*$^{-/-}$ (Fig. 5C), consistent with the increased initial and steady-state P_r.

Loss of Rac1 impacts delay and temporal precision of AP firing in response to SAM stimuli

Animal vocalization including human speech is characterized by rapid amplitude modulations (Joris et al., 2004). These amplitude modulations can be mimicked by sinusoidal amplitude-modulated stimuli (SAM) which will produce periodic fluctuations in the firing rates of the calyx of Held (Mc Laughlin et al., 2008; Tolnai et al., 2008). Therefore, different SAM frequencies will differentially stress SV release and recovery mechanisms and can be used to relate the observed changes in synaptic strength and SV recovery to potential impacts on auditory signaling in the *Rac1*$^{-/-}$ calyces. Using *in vivo* responses to SAM stimuli (Tolnai et al., 2008) which contained modulation frequencies between 20 Hz and 2000 Hz as templates for afferent fiber stimulation, we recorded postsynaptic APs in loose-patch configuration (Fig. 6). First, we analyzed how successful a presynaptic stimulus resulted in a postsynaptic AP to assess the reliability of synaptic transmission and found no difference between *Rac1*$^{+/+}$ and *Rac1*$^{-/-}$ independent of modulation frequency (Fig. 6B1). Since temporal precision is crucial in auditory signaling, we then analyzed if the loss of Rac1 impacted the temporal precision of AP generation by calculating the standard deviation of AP delays (AP jitter). Independent of modulation frequency, temporal precision was unchanged when analyzed for the complete stimulus (Fig. 6B2). However, the previous analysis showed that EPSC onset delay and synchronicity were only affected at high stimulation frequencies. Since the SAM stimuli generate periods of high firing activity interspersed with periods of low activity, we tested how preceding activity

influenced AP jitter and AP delay. First, we used the preceding interspike interval (ISI) as an estimate of preceding activity and calculated AP jitter and AP delay for different ISIs (Fig. 6C1). Both, AP jitter and AP delay were comparable between *Rac1*$^{+/+}$ and *Rac1*$^{-/-}$ for most ISIs but AP delay in *Rac1*$^{-/-}$ increased slightly at short ISIs. Previous studies showed that EPSC/EPSP amplitudes, and subsequent AP generation, are influenced by preceding neuronal activity (Haustein et al., 2008; Englitz et al., 2009; Lorteije et al., 2009; Sonntag et al., 2011; Yang and Xu-Friedman, 2015; Ghanbari et al., 2020). Since our previous analysis only considered the last ISI and thus is an incomplete estimate of preceding activity, we estimated activity levels by calculating the sum of all preceding APs weighted by their distance to the AP under observation (Fig. 6C2). Using this method, we found that AP jitter was similar between *Rac1*$^{+/+}$ and *Rac1*$^{-/-}$ for low to moderate activity levels but diverged at increasing activity levels with *Rac1*$^{-/-}$ showing higher AP jitter (*Rac1*$^{+/+}$ = 65 ± 32 µs vs. *Rac1*$^{-/-}$ = 99 ± 62 µs, p = 1.5e-5 µs, n = 14/18). Similarly, AP delays were similar for low activity levels, but increased more in *Rac1*$^{-/-}$ with increasing activity (*Rac1*$^{+/+}$ = 110 ± 52 µs vs. *Rac1*$^{-/-}$ = 158 ± 101 µs, p = 0.03). These data suggest that the activity-dependent increase in EPSC onset and reduction in EPSC synchronicity in *Rac1*$^{-/-}$ at high stimulation frequencies translates into a small but consistent increase in AP delays and AP jitter.

Discussion

By ablating Rac1 at the calyx of Held after hearing onset, we identified the presynaptic roles of Rac1 in regulating synaptic transmission and plasticity in a native neuronal circuit. Based on our data we conclude that presynaptic Rac1 is a key regulator of synaptic strength and RRP replenishment through SV priming steps that control intrinsic SV P_r. Therefore, we propose that presynaptic Rac1 is a critical regulator for encoding information by neuronal circuits.

Rac1 regulates P_r and RRP recovery

Our finding that Rac1 is a negative regulator of P_r is in contrast with a recent study in primary cultured hippocampal neurons that concluded presynaptic Rac1 does not regulate P_r (O'neil et al., 2021). Multiple reasons may explain these differences. One cause may be due to the specific conditions of a native neuronal circuit that are not replicated in *in vitro* cultured neuronal circuits. We specifically abated Rac1 at a distinct developmental time point, two days after hearing onset where neuronal circuit properties are well defined and the calyx of Held is functionally mature (Englitz et al., 2009; Sonntag et al., 2009, 2011; Borst and Soria Van Hoeve, 2012). Although Rac1 was ablated at 10 days *in vitro* (O'neil et al., 2021), the corresponding developmental stage to *in vivo* hippocampal neurons is unclear. In addition, it is unknown to what extent the artificial *in vitro* circuit properties determine synaptic transmission and plasticity characteristics. Another critical difference between our studies was the recording condition. We used 1.2 mM $[Ca^{2+}]_{ext}$ and physiological temperatures to mimic *in vivo* conditions (Lorteije et al., 2009; Borst, 2010; Forsberg et al., 2019), while 2 mM $[Ca^{2+}]_{ext}$ at room temperature was used in the prior study. As a result, we observed an initial P_r ~0.1 with no P_r higher than 0.15 in *Rac1*$^{+/+}$ calyces and a two-fold increase following Rac1 ablation. However, in the cultured neurons, the initial P_r was ~0.4 in *Rac1*$^{+/+}$ with many values exceeding 0.5 in both excitatory and inhibitory neurons. Therefore, it is likely that in cultured neurons, P_r was close to maximum or at maximum thereby masking any potential increases in P_r in *Rac1*$^{-/-}$ neurons. In addition, many regulatory steps in the SV lifecycle that influence P_r are temperature-dependent (Chanaday and Kavalali,

2020), and in mouse hippocampal synapses actin-dependent synaptic release enhancement was only detected at physiological temperatures (Jensen et al., 2007).

The RRP size is a critical determinant of synaptic strength that maintains synaptic transmission during ongoing stimulation. Since the RRP size varies with stimulation rates (Thanawala and Regehr, 2013, 2016; Neher, 2015), SV replenishment is key in regulating RRP size. SV replenishment rates are typically estimated by two methods (Hallermann and Silver, 2013; Neher, 2015): i) SV replenishment rates during ongoing stimulation which corresponds to the slope of the line fit using the SMN plot, or ii) RRP replenishment rates that are estimated by plotting the fraction of recovered RRP or initial ESPC amplitudes as a function of interstimulus intervals following RRP depletion. Subsequently, the RRP replenishment rates are described by the time constants of fits. Using the slope of the line fit, we found that *Rac1*$^{-/-}$ calyces had faster SV replenishment rates and larger steady-state EPSC amplitudes at 50 Hz train stimulation which is similar to observations in primary hippocampal cultures at 20 and 40 Hz train stimulation (O'neil et al., 2021). In contrast, at 500 Hz train stimulation, there was no difference between *Rac1*$^{+/+}$ and *Rac1*$^{-/-}$ calyces in SV replenishment rates or steady-state EPSC amplitudes. However, RRP replenishment was best fit with a bi-exponential fit, with a faster slow component in *Rac1*$^{-/-}$ (1.8s vs 2.4s), but no difference in fast component (~40 ms) or relative contribution of each time constant. These observations run counter to numerous observations demonstrating that increasing activity rates results in faster SV replenishment and shorter RRP recovery time constants (Wang and Kaczmarek, 1998; Hallermann and Silver, 2013). However, the fractional recovery in *Rac1*$^{-/-}$ calyces at 50 ms recovery interval was ~ 2 fold higher and steady-state EPSC levels were similar at 500 Hz and larger at 50 Hz stimulation frequency despite increased depletion in *Rac1*$^{-/-}$ calyces. Therefore, if defined as fractional recovery of the initial RRP rather than ongoing SV replenishment during stimulation this would indicate faster SV replenishment rates in *Rac1*$^{-/-}$ calyces at 500 Hz stimulation frequency.

Replenishment rates depend on the release site vacancy which depends on P_r, therefore P_r is critical in controlling SV replenishment (Vere-Jones, 1966; Quastel, 1997; Scheuss and Neher, 2001; Zucker and Regehr, 2002; Neher, 2010; Pulido and Marty, 2017; Kusick et al., 2020; Tanaka et al., 2021). Analysis of steady-state P_r by two independent methods demonstrated that the steady-state P_r was elevated in *Rac1*$^{-/-}$ calyces. Since the interstimulus intervals at both 50 Hz (20 ms) and 500 Hz (2 ms) stimulation frequency are shorter than the fast RRP replenishment time constant, this indicates that Rac1 regulation of P_r controls SV replenishment on the time scale of hundreds of microseconds which is faster than known SV recruitment steps. To explain our conclusion, we assume two synapses with different P_r (*Rac1*$^{+/+}$ with 0.1 and *Rac1*$^{-/-}$ with 0.2) and steady-state RRP size (*Rac1*$^{+/+}$ with 20 SVs and *Rac1*$^{-/-}$ with 10 SVs), but similar steady-state EPSCs during ongoing stimulation (500 Hz condition). In this scenario, both synapses would replenish the same absolute number of SV, since each synapse will release 2 SVs per stimulus (20*0.1 vs. 10*0.2) and these 2 SVs will be replenished between stimuli. Therefore, when calculating the SV replenishment rate relative to total RRP at rest using back extrapolation, the SV replenishment rates would be similar as the absolute replenishment and total RRP are the same. However, if one defines SV replenishment as the proportion of the steady-state RRP relative to the initial RRP, then the high-P_r synapse would have higher SV replenishment rates compared to the low P_r synapse (20 % of the steady-state RRP vs. 10% of the steady-state RRP). In contrast, at 50 Hz stimulation condition, steady-state EPSCs were larger in the high P_r (*Rac1*$^{-/-}$) compared to low P_r synapse (*Rac1*$^{+/+}$). Assuming a similar steady-state RRP (e.g. 20 SVs), the high P_r synapses would release and replenish more SVs per stimulus compared to the low P_r synapse (0.1*20 = 2 SVs vs. 0.2*20 = 4 SVs). Therefore, the SV replenishment rate calculated using back extrapolation will be faster in the high P_r synapse although the total RRP is the same.

Rac1 regulation of SV Priming control SV P_r and RRP recovery

In response to APs, synapse P_r is regulated by SV fusogenecity, the fusion willingness of an SV (intrinsic SV P_r), and the localization of SVs relative to VGCCs (Schneggenburger and Rosenmund, 2015). SV priming controls SV P_r through two steps, molecular priming and positional priming (Neher and Brose, 2018). Molecular priming controls intrinsic SV P_r by regulating SV fusogenicity through SV docking states which represent the conversion from loose-state (LS) to tight-state (TS) and the tightness of the TS state (Neher and Brose, 2018). Positional priming regulates the proximity of SVs to VGCCs to control SV P_r independent of intrinsic SV P_r (Neher, 2010). Based on our findings of how the loss of Rac1 impacted mEPSCs rates and AP-evoked release, we propose that Rac1 regulates SV P_r and RRP recovery at the level of molecular priming. Since mEPSCs are independent of VGCCs (Kavalali, 2014, 2020) they function as readouts of molecular priming, with increased mEPSC rates corresponding to increased SV fusogenecity (Basu et al., 2007; Schotten et al., 2015; Dong et al., 2018). In the absence of Rac1, mESPC rates were increased in the presence of Cd^{2+} which rules out any Cav2.1 channel contribution. Furthermore, the increase in SV P_r in *Rac1*$^{-/-}$ was not caused by changes in SV docking or RRP size since both AZ ultrastructure and initial RRP size measured by AP train stimulation was unchanged.

AP-evoked EPSCs in *Rac1*$^{-/-}$ calyces were delayed and less synchronous particularly at high firing rates indicating that SVs were less tightly coupled in *Rac1*$^{-/-}$ calyces. The EPSC onset delay which is an estimate of positional priming includes two components: conduction delay, the time from afferent fiber stimulation to the presynaptic AP, and SV release delay, the time between presynaptic AP and the onset of the EPSC which is mainly dependent on the distance between SVs to VGCCs (Fedchyshyn and Wang, 2007). Since Rac1 regulates actin dynamics, the loss of Rac1 may prolong conduction delay during train stimuli that obscured Rac1's role in positional priming. If the conduction delay was solely responsible for the increase in onset delays, AP-evoked release kinetics would be unchanged. However, both onset delay and

release synchronicity were activity-dependent in *Rac1*$^{-/-}$ calyces suggesting a change in SV release kinetics. Since after hearing onset, the calyx of Held utilizes nanodomain release which targets SVs within ~25 nm of the Cav2.1 channels (Fedchyshyn and Wang, 2005; Chen et al., 2015), the decrease in SV release synchronicity suggests that more distal SVs were released in Rac1$^{-/-}$.

Another plausible scenario is that presynaptic APs in *Rac1*$^{-/-}$ were broader and contributed to increased P_r. However, using TEA, a Kv3 channel blocker, to broaden the presynaptic AP impairs high-frequency firing at the calyx of Held (Wang and Kaczmarek, 1998; Wang et al., 1998; Johnston et al., 2010). Furthermore, presynaptic deletion of Kv3.3 channels broadens APs and increased P_r but enhanced short-term depression and decreased steady-state EPSC amplitudes (Richardson et al., 2022). Since *Rac1*$^{-/-}$ had similar or larger steady-state EPSCs, were able to follow high-frequency stimulation, and the intrinsic SV fusogenicity *Rac1*$^{-/-}$ was increased, it is unlikely that broadened APs contributed to increased P_r.

Loss of Rac1 might impact endocytosis through changes in actin signaling (Wu and Chan, 2022). However, at the calyx of Held, the endocytic role of F-actin appears to be negligible as actin depolymerization using latrunculin did not affect endocytosis (Eguchi et al., 2017; Babu et al., 2020). Furthermore, endocytosis acts on a time scale of seconds and would be too slow to contribute to SV replenishment during train stimulation (Armbruster and Ryan, 2011). Although ultrafast endocytosis occurs on a timescale of tens of milliseconds, it is F-actin dependent, and SV reformation is too slow as it takes tens of seconds (Watanabe et al., 2013a, 2013b). In addition, endocytosis is postulated to play a role in release site clearance (Neher, 2010)as the perturbation of endocytosis increases the rate of synaptic depression and slows RRP recovery (Hua et al., 2013) which we did not observe in the *Rac1*$^{-/-}$ calyces.

Rac1 regulation of auditory signaling and information processing.

The ability to accurately encode sound information requires synaptic transmission in the lower auditory brainstem to drive and sustain precise AP firing over rapid and large fluctuations of AP

firing rates up to the kilohertz range (Grothe et al., 2010; Borst and Soria Van Hoeve, 2012; Friauf et al., 2015). The calyx of Held/MNTB synapse is a safe and reliable synaptic relay that transforms afferent AP spike patterns from the cochlear nucleus (CN) into precisely timed inhibition to several mono- and binaural cell groups (Spirou et al., 1990; Scheuss and Neher, 2001; Joris et al., 2004; Englitz et al., 2009; Lorteije et al., 2009; Sonntag et al., 2011). The use of SAM stimuli which mimics the neuronal response to environmental sounds (Joris et al., 2004; Tolnai et al., 2008) suggests that loss of Rac1 did not deteriorate the faithful auditory signaling properties over different amplitude modulation frequencies. However, we found that the increase in EPSC onset and decrease in SV release synchronicity in *Rac1*$^{-/-}$ translated into larger AP delay and AP jitter at high activity levels. Although the absolute changes were modest, the need for immaculate temporal precision in the auditory brainstem might cause a more severe impact in downstream nuclei such as the lateral and medial superior olive. Since the calyx of Held generates suprathreshold EPSCs even under short-term depression (Lorteije et al., 2009; Lorteije and Borst, 2011), the impact of P_r changes caused by Rac1 ablation will be modest in affecting MNTB firing, but likely more substantial in other synapses in the SPON, MSO, or LSO that operate close to AP threshold or rely on synaptic integration to encode information.

Ideas and speculation

Rac1 regulation of F-actin dynamics controls SV priming

F-actin is implicated in the regulation of several SV life cycle steps which could impact SV replenishment rates (Morales et al., 2000; Sakaba and Neher, 2003; Cingolani and Goda, 2008; Waites et al., 2011; Lee et al., 2012, 2013; Montesinos et al., 2015; Rust and Maritzen, 2015). Specifically, F-actin has been proposed to act as a physical barrier within the presynaptic AZ (Cingolani and Goda, 2008) as the transient application of latrunculin increased P_r and mEPSC rates (Morales et al., 2000). Studies in which Septin 5 (Yang et al., 2010) or the actin cytoskeleton was disrupted (Lee et al., 2012) are in support of the idea of F-actin as a structural barrier impacting positional priming. However, F-action may act as a vertical barrier to impact

molecular priming (Yang et al., 2010). Therefore, since Rac1 regulates molecular priming, we propose that Rac1's regulation of F-actin acts as a vertical barrier to regulate the conversion from LS to TS and the tightness of the TS (Fig. 7). In our model, the loss of Rac1 results in local actin depolymerization in the AZ which increases SV fusogenicity by placing SVs in closer proximity to the AZ which increases the LS to TS transition rate and TS tightening which increases P_r. In support of our model, increased P_r has been demonstrated to correlate with shortened tethering filaments that resulted in SVs positioned more closely to the presynaptic membrane (Jung et al., 2021). Since GIT proteins (Montesinos et al., 2015), Arp2/3 (O'neil et al., 2021), and Piccolo (Waites et al., 2011) are regulators of F-actin dynamics and control P_r this suggests that F-actin signaling cascades at the AZ regulate P_r potentially through molecular priming and/or positional priming. More importantly, this suggests that molecules regulating F-actin dynamics at the AZ could be key regulators of SV replenishment independent of facilitation sensors. However, to determine if F-actin levels are reduced specifically within 20 nm at the AZ would require the development of new tools and techniques to carry out these future experiments.

Mutations in *Rac1* that result in loss or gain of function are associated with intellectual disability (Reijnders et al., 2017; Zamboni et al., 2018). While much attention has focused on *Rac1* dysregulation in the dendritic compartment or neuronal development, our work demonstrates that presynaptic loss of *Rac1* increases P_r independent of its developmental role. Therefore, human mutations in *Rac1* might affect P_r and excitation-inhibition balance and thereby alter plasticity in many different neuronal circuits associated with neurological disorders and addiction (Dietz et al., 2012; Bai et al., 2015; Wright et al., 2020).

Methods

Key Resources Table

Reagent type (species) or resource	Designation	Source or reference	Identifiers	Additional information
strain (*Mus musculus*)	Rac1^{tm1Djk}/J (Rac1$^{flox/flox}$)	Jackson Laboratory Glogauer et al. (2003)	RRID:IMSR_JAX:005550	either sex
antibody (rabbit polyclonal)	rabbit anti-GFP	Abcam	Cat# ab6556 RRID:AB_305564	EM (0.1 µg/mL)
antibody (donkey polyclonal)	6 nm colloidal Gold-AffiniPure Donkey anti rabbit IgG	Jackson ImmunoResearch	Cat# 711-195-152 RRID:AB_2340609	EM (1:100)
sequence-based-reagent	primer: 5'-TCC AAT CTG TGC TGC CCA TC-3'	Glogauer et al. (2003)		
sequence-based-reagent	primer: 5'-GAT GCT TCT AGG GGT GAG CC-3'	Glogauer et al. (2003)		
Recombinant DNA reagent (viral vector)	HdAd 28E4 hsyn iCre EGFP	Samuel M. Young, Jr., University of Iowa		
Recombinant DNA reagent (viral vector)	HdAd 28E4 hsyn iCre mEGFP	Samuel M. Young, Jr., University of Iowa		
Recombinant DNA reagent (viral vector)	HdAd 28E4 hsyn mEGFP	Samuel M. Young, Jr., University of Iowa		
chemical compound/drug	kynurenic acid	Tocris Bioscience	Cat# 0223	
chemical compound/drug	lidocaine N-ethyl bromide (QX-314)	Sigma Aldrich	Cat# L5783	
chemical compound/drug	D-AP5	Tocris Bioscience	Cat# 0106	
chemical compound/drug	(-)-bicuculline methochloride	Tocris Bioscience	Cat# 0131	
chemical compound/drug	strychnine hydrochloride	Tocris Bioscience	Cat# 2785	
chemical compound/drug	tetraethylammonium chloride	Sigma Aldrich	Cat# T-2265	

chemical compound/drug	tetrodotoxin	Alomone labs	Cat# T-550	
chemical compound/drug	Cadmium chloride hemi(pentahydrate)	Sigma Aldrich	Cat# C3141	
software/algorithm	Matlab	The Mathworks	RRID:SCR_001622; v9.10	
software/algorithm	Patchmaster	HEKA; Harvard Bioscience	RRID:SCR_000034; v2x90.2	
software/algorithm	Igor Pro	Wavemetrics	RRID:SCR_000325; v6.37	
software/algorithm	Fiji	https://fiji.sc/	RRID:SCR_002285	
software/algorithm	Patcher's Power Tools	Max Planck Institute for Biophysical Chemistry; Gottingen; Germany	RRID:SCR_001950; v2.19	
software/algorithm	StereoDrive	Neurostar	N/A; v3.1.5	
software/algorithm	Live Acquisition	Thermo Fisher Scientific	N/A; v2.1.0.10	
software/algorithm	Neuromatic	Rothman and Silver (2018)	RRID:SCR_004186	

Animals

All experiments were performed following animal welfare laws and approved by the Institutional Committee for Care and Use of Animals at the University of Iowa (PHS Assurance No. D16-00009 (A3021-01) (Animal Protocol 0021952) and complied with accepted ethical best practices. Animals were housed at a 12-hour light/dark cycle and had access to food and water ad libitum. Experiments were performed on Rac1^{tm1Djk} (*Rac1*$^{fl/fl}$) mice (Glogauer et al., 2003; RRID:IMSR_JAX: 005550, The Jackson Laboratory, Bar Harbor, USA) of either sex. Animals of this line possess a *loxP* site flanking exon 1 of the *Rac1* gene disrupting Rac1 expression after recombination mediated by Cre recombinase. Genotyping was performed using PCR-amplification with the following primers 5'-TCC AAT CTG TGC TGC CCA TC-3' and 5'-GAT GCT TCT AGG GGT GAG CC-3' and amplification products (*Rac1*$^{fl/fl}$: 242 bp, wildtype: 115 bp) were separated gel electrophoresis on a 1.5% agarose gel (Glogauer et al., 2003). Viral vectors

were injected at postnatal day 14 (P14) and experiments were performed at P28-30. All available measures were taken to minimize animal pain and suffering.

DNA construct and recombinant viral vector production

Helper-dependent adenoviral vectors (HdAd) expressing a codon-optimized Cre recombinase (Cre) (Shimshek et al., 2002) were produced as previously described (Montesinos et al., 2016; Lübbert et al., 2017). These HdAd vectors contain two independent transgene cassettes that independently express Cre recombinase and EGFP or myristoylated EGFP (mEGFP) under the control of 470 bp human synapsin promoter (Lübbert et al., 2017). In brief, the expression cassette with Cre recombinase was cloned into the pdelta28E4 SynEGFP plasmid using the *Asc*I enzyme digestion site. The final plasmid has been modified to also contain a separate EGFP or myristoylated EGFP (mEGFP) expression cassette. Then, the pHAD plasmid was linearized by *PmeI* enzyme to expose the ends of the 5' and 3' inverted terminal repeats (ITRs) and transfected into 116 producer cells (Profection® Mammalian Transfection System, Promega, Madison, WI, USA). Helper virus (HV) was added the following day for HdAd production. Forty-eight hours postinfection, after cytopathic effects have taken place, cells were subjected to three freeze/thaw cycles for lysis and release of the viral particles. HdAd was purified by CsCl ultracentrifugation. HdAd was stored at -80 °C in storage buffer (10 mM HEPES, 1 mM $MgCl_2$, 250 mM sucrose, pH 7.4).

Virus injections

Virus injections at P14 were performed as previously described (Lübbert et al., 2019). Briefly, mice were anesthetized with 5% isoflurane inhalation and anesthesia was maintained with 2% isoflurane throughout the procedure. Subcutaneous injection of physiological saline, lidocaine, bupivacaine, and meloxicam was used to treat loss of liquid and alleviate pain. The injection site was determined using the Stereodrive software (Neurostar) and corrected for head orientation and tilt. A small hole (diameter <1 mm) was drilled into the skull using a foot-pedal controlled drill MH-170 (Foredom). The virus solution was injected via a glass pipet (Drummond) at a rate of

100 nL/min with a nanoliter injector (NanoW, Neurostar). Following the injection, the glass needle was left in place for 1 min to dissipate the pressure and then slowly retracted. Animals were then placed under an infrared heat lamp and allowed to recover before being returned to their respective cages with their mother.

Confocal imaging and reconstruction of presynaptic terminals

For reconstruction of the calyx of Held terminals, animals were injected with viral vectors expressing either mEGFP (yielding *Rac1*$^{+/+}$) or Cre recombinase and mEGFP (yielding *Rac1*$^{-/-}$). Mice were anesthetized with an intraperitoneal injection of tribromoethanol (250 mg/kg body weight) and transcardially perfused with ice-cold 0.1 M phosphate buffer (PB, pH 7.4) followed by 4% paraformaldehyde (PFA) in 0.1 M PB. Brains were removed and post-fixed overnight in 4% PFA solution at 4°C. The next day, brains were sliced into 40 µm sections on a Leica VT1200 vibratome. mEGFP positive slices were identified and mounted on cover slips with Aqua Polymount (Polysciences, Inc., Warrington, PA, USA). Confocal images were acquired with a Zeiss LSM 700 or 880 confocal scanning microscope using a 63x/1.3 NA Apochromat multi-immersion objective. Image stacks were collected using 0.44 um plane line scans with line average of four times. Images were processed using Fiji (Schindelin et al., 2012, http://fiji.sc., RRID:SCR 002285). Calyx reconstructions were performed blind to genotype using Imaris Measurement Pro (BitPlane) using automatic signal detection manual curation in single planes in Z-stack confocal images as previously described (Radulovic et al., 2020).

Electron microscopy

Preembedding immuno-electron microscopy was performed as previously described (Montesinos et al., 2015; Dong et al., 2018). Briefly, *Rac*$^{fl/fl}$ mice injected at P14 with HdAd co-expressing Cre-recombinase and EGFP were anesthetized and perfused transcardially at P28 with phosphate-buffered saline (PBS, 150 mM NaCl, 25 mM Sørensen's phosphate buffer, pH 7.4) followed by fixative solution for 7-9 min containing 4% PFA, 0.5% glutaraldehyde, and 0.2% picric acid in 100 mM Sørensen's phosphate buffer (PB, pH 7.4). Brains were post-fixed

with 4% PFA in PB overnight and 50-µm coronal sections of the brainstem were obtained on a vibratome (Leica VT1200S). Expression of EGFP at the calyx of Held terminals was visualized using an epifluorescence inverted microscope (CKX41, Olympus) equipped with an XCite Series 120Q lamp (Excelitas Technologies), and only those samples showing EGFP were further processed. After washing with PB, sections were cryoprotected with 10%, 20%, and 30% sucrose in PB and submersed into liquid nitrogen, then thawed. Sections were incubated in a blocking solution containing 10% normal goat serum (NGS), 1% fish skin gelatin (FSG), in 50 mM Tris-buffered saline (TBS, 150 mM NaCl, 50 mM Tris, pH 7.4) for 1h, and incubated with an anti-GFP antibody (0.1 µg/mL, ab6556, Abcam, RRID: AB_305564) diluted in TBS containing 1% NGS, 0.1% FSG plus 0.05% NaN_3 at 4°C for 48h. After washing with TBS, sections were incubated overnight in nanogold conjugated donkey anti-rabbit IgG (1:100, Jackson Immunoresearch, RRID: AB_2340609) diluted in TBS containing 1% NGS and 0.1% FSG. Immunogold-labeled sections were washed in PBS, briefly fixed with 1% glutaraldehyde in PBS, and silver intensified using an HQ silver intensification kit (Nanoprobe). After washing with PB, sections were treated with 0.5% OsO_4 in 0.1 M PB for 20 min, en-bloc stained with 1% uranyl acetate, dehydrated and flat embedded in Durcupan resin (Sigma-Aldrich). After trimming out the MNTB region, ultrathin sections were prepared with 40 nm-thickness using an ultramicrotome (EM UC7, Leica). Sections were counterstained with uranyl acetate and lead citrate and examined in a Tecnai G2 Spirit BioTwin transmission electron microscope (Thermo Fisher Scientific) at 100 kV acceleration voltage. Images were taken with a Veleta CCD camera (Olympus) operated by TIA software (Thermo Fisher Scientific). Images used for quantification were taken at 60 000x magnification.

TEM image analysis

Calyces positive for Cre expression (*Rac1*$^{-/-}$) were identified by immunogold labeling with an anti-GFP antibody and compared to EGFP-negative terminals (*Rac1*$^{+/+}$) in the same slice or calyces in the wildtype sample. All TEM data were analyzed using Fiji imaging analysis software

(Schindelin et al., 2012). Each presynaptic active zone (AZ) was defined as the membrane directly opposing the postsynaptic density, and the length of each AZ was measured. Vesicles within 200 nm from each AZ were manually selected and their distances relative to the AZ were calculated using a 32-bit Euclidean distance map generated from the AZ. For data analysis, vesicle distances were binned every 5 nm and counted (Montesinos et al., 2015; Dong et al., 2018). Vesicles less than 5 nm from the AZ were considered “docked”. Three animals for each condition and ~40 AZs per animal were analyzed. Analysis was performed blind to genotype independently by three researchers and results were averaged.

Electrophysiology

Acute coronal brainstem slices (~200 µm) containing the MNTB were prepared as previously described (Chen et al., 2013; Thomas et al., 2019). Briefly, after decapitation of the animal, the brain was immersed in low-calcium artificial cerebrospinal fluid (aCSF) solution containing (in mM): 125 NaCl, 2.5 KCl, 3 $MgCl_2$, 0.1 $CaCl_2$, 10 glucose, 25 $NaHCO_3$, 1.25 NaH_2PO_4, 0.4 L-ascorbic acid, 3 myo-inositol, and 2 Na-pyruvate, pH 7.3–7.4). Brain slices were obtained using a Leica VT 1200S vibratome equipped with zirconia ceramic blades (EF-INZ10, Cadence Blades) as previously described. The blade was advanced at a speed of 20-50 µm/s. Slices were immediately transferred to an incubation beaker containing standard extracellular solution (same as above but using 1 mM $MgCl_2$ and 1.2 mM $CaCl_2$) at ~37°C and continuously bubbled with 95% O_2–5% CO_2. After approximately 45 min of incubation, slices were transferred to a recording chamber with the same saline solution at physiological temperature (~37°C).

Electrical stimulation of afferent fibers was performed as previously described (Forsythe and Barnes-Davies, 1993a, 1993b). Briefly, a bipolar platinum-iridium electrode was positioned medially of the MNTB to stimulate afferent fibers (FHC, Model MX214EP). Postsynaptic MNTB neurons were whole-cell voltage-clamped at −60 mV using an EPC10/2 amplifier controlled by Patchmaster Software (version 2x90.2, HEKA Elektronik, RRID:SCR_000034). Slices were continuously perfused with normal aCSF solution at a rate of 1 mL/min and visualized by an

upright microscope (BX51WI, Olympus) through a 60x water-immersion objective (LUMPlanFL N, Olympus) and an EMCCD camera (Andor Luca S, Oxford Instruments). To identify calyces expressing Cre-recombinase and EGFP, the slice was illuminated at an excitation wavelength of 480 nm using a Polychrome V xenon bulb monochromator (TILL Photonics). For whole-cell voltage-clamp recordings, the standard extracellular solution was supplemented with 1 mM kynurenic acid to avoid saturation of postsynaptic AMPA receptors, 50 µM D-AP-5 to block NMDA receptors, and 20 µM bicuculline and 5 µM strychnine to block inhibitory GABA- and glycine receptors, respectively (all Tocris Bioscience). Patch pipettes had a resistance of ~3–4 MΩ and were filled with the following (in mM): 130 Cs-gluconate, 20 tetraethylammonium (TEA)-Cl, 10 HEPES, 5 Na_2-phosphocreatine, 4 Mg-ATP, 0.3 Na-GTP, 6 QX-314, and 5 EGTA, pH 7.2 (315 mOsm. Reported voltages are uncorrected for a calculated liquid junction potential of 13 mV. For loose-patch recordings, the extracellular solution was supplemented with 20 µM bicuculline and 5 µM strychnine, and the patch pipettes were filled with aCSF. To simulate *in vivo* activity levels, afferent fibers were stimulated with activity patterns previously recorded *in vivo* in response to sinusoidal amplitude-modulated (SAM) sound stimulation (Tolnai et al., 2008).

mEPSCs were recorded with the same aCSF supplemented with 50 mM D-AP5, 20 µM bicuculline, 5 µM strychnine, 1 µM TTX, and 20 mM TEA. In a subset of *Rac1*$^{-/-}$ recordings, Cd^{2+} (cadmium chloride), a non-selective Ca^{2+} channel blocker was flushed in during recordings to determine the impact of VGCC on spontaneous SV release. The baseline mEPSC frequency was established by recording each cell for at least one minute before Cd^{2+} was flushed in via the bath perfusion. MNTB principal neurons were whole-cell voltage-clamped at -80 mV and recorded until enough mEPSCs (>25) were recorded. Overlapping events were excluded from the analysis.

Data were acquired at a sampling rate of 100 kHz and lowpass filtered at 6 kHz. Series resistance (3–8 MΩ) was compensated online to <3 MΩ, except for mEPSC recordings where

series resistance (<9 MΩ) was not compensated. All experiments were performed at near-physiological temperature (36-37°C) and the temperature was maintained by a heated bath chamber (HCS, ALA Scientific Instruments) and perfusion system (HPC-2, ALA Scientific Instruments). The temperature of the bath solution was monitored during the experiment using a glass-coated micro thermistor.

Electrophysiological data analysis

Electrophysiological data were imported to Matlab (version 9.10; The Mathworks, RRID:SCR_001622) using a custom-modified version of sigTool (Lidierth, 2009) and Igor Pro (version 8.0.4.2, Wavemetrics, RRID:SCR_000325) equipped with Patcher's Power Tools (version 2.19, RRID:SCR_001950) and NeuroMatic (Rothman and Silver, 2018, RRID:SCR_004186), and analyzed offline with custom-written functions in Matlab and IgorPro. The remaining series resistance was compensated offline to 0 MΩ with a time lag of 10 µs (Traynelis, 1998). EPSC amplitudes were measured as peak amplitude minus baseline preceding the EPSC. RRP size and P_r were calculated using the EQ method (Elmqvist and Quastel, 1965), back-extrapolation method (SMN with correction, Neher, 2015), and NpRf model (Thanawala and Regehr, 2016) as previously described (Lübbert et al., 2019). Steady-state Pr was calculated by dividing the steady-state EPSC by the RRP size corrected for partial depletion: $Pr_{ss} = EPSC_{ss}/(RRP \cdot EPSC_{ss}/EPSC_1)$. Onset time of EPSCs was determined by fitting a Boltzmann function to the EPSC rising flank and calculating the time point of maximum curvature, as described previously (Fedchyshyn and Wang, 2007). The duration between stimulus and EPSC onset was defined as EPSC onset delay. Synchronicity of SV release was estimated for individual EPSCs by dividing their EPSC amplitude by their EPSC charge.

Recordings of mEPSCs were analyzed using NeuroMatic in Igor Pro. Potential events were detected when exceeding an amplitude threshold at 4-6 times the standard deviation of the baseline and all events were manually curated to exclude false positives. Rise time was

measured between 10% and 90% of the amplitude. Full width at half-maximal amplitude (FWHM) was measured at 50% amplitude.

Recovery of SVs was estimated by non-linear least-square fits for single EPSC and RRP recovery. Both types of recovery were best fit with a bi-exponential function of the form:

$$A\left(1 - f\left(e^{-\frac{t}{\tau_{d1}}}\right) + (1-f)\left(e^{-\frac{t}{\tau_{d2}}}\right)\right)$$

with variable A constraint to 1 when fitting fractional recovery. An F-test was used to statistically determine the better fit as described previously. Fractional recovery of the first EPSC was calculated as $(EPSC_{test}^{1} - EPSC_{dep}^{ss})/(EPSC_{dep}^{1} - EPSC_{dep}^{ss})$ where $EPSC_{test}^{1}$ is the amplitude of the first EPSC of the test train, $EPSC_{dep}^{ss}$ the steady-state amplitude of the depleting train and $EPSC_{dep}^{1}$ the amplitude of the first EPSC of the depleting train.

To estimate preceding neuronal activity during SAM stimulation, we calculated the interspike interval (ISI) as the distance to the preceding AP. For the analysis of AP responses during SAM stimulation, we used the preceding ISI to estimate the influence of previous activity during SAM recordings. Since short-term plasticity can extend well beyond the last ISI, we also estimated preceding activity by calculating the sum of all preceding events with each event weighted by its distance to the AP under observation. This weighting was implemented as a single-exponential decaying function, emphasizing temporally close events over more distant ones (Sonntag et al., 2009; Keine et al., 2016). The time constant was set to 30 ms, consistent with previous reports (Yang and Xu-Friedman, 2015). The calculation was also performed with time constants of 10 ms and 100 ms yielding similar results.

Experimental design and statistical analysis

For the electrophysiological data analysis and morphological reconstruction, individual neurons were considered independent samples. For thin-section TEM analysis, AZs were considered independent samples (244 total AZs, 6 animals, ~40 AZs each). Statistical analysis was conducted in MATLAB (version 9.4, RRID:SCR_001622) and GraphPad Prism

(RRID:SCR_002798). Data distributions were tested for Gaussianity using the Shapiro-Wilk test. To compare two groups, a two-tailed unpaired Student's t-test with Welch's correction (normal distribution) or a two-tailed Mann-Whitney *U* test (non-normal distribution) was used. To compare more than two groups with within-subject factors, an RM ANOVA was performed, and p-values were Bonferroni-adjusted for multiple comparisons. Fits to data were subject to F-tests to determine the better model (mono- or biexponential) and for comparison between groups. For interpretation of all statistical tests, a p-value of 0.05 was deemed significant. Effect sizes were calculated using the MES toolbox in MATLAB (Hentschke and Stüttgen, 2011) and are reported as Cohen's U_1 for two-sample comparison and eta-squared (η^2) for RM ANOVA. No statistical test was performed to pre-determine sample sizes. Exact p-values, test statistics, and effect sizes for all statistical comparisons are summarized in supplemental tables. Boxplots in the figures show median, interquartile, and minimum/maximum within 1.5 times the interquartile range. Average data in the text are reported as mean ± standard deviation.

Data and software accessibility

All experimental data and custom-written software central to the conclusion of this study are available at http://dx.doi.org/10.17632/c4b7gn8bh7 under the terms of the Creative Commons Attribution 4.0 License (CC BY 4.0).

Acknowledgments

We would like to thank the members of the Young lab for their comments on the manuscript. This work was supported by the National Institute of Deafness and Other Communication Disorders (R01 DC014093) National Institute of Neurological Disorders and Stroke (R01NS110742), the University of Iowa (SMY), and a German Research Foundation postdoctoral fellowship (DFG 420075000) (CK).

Competing interests

The authors declare no competing interests.

References

Alabi ARA, Tsien RW (2012) Synaptic vesicle pools and dynamics. Cold Spring Harb Perspect Biol 4:a013680–a013680.

Armbruster M, Ryan TA (2011) Synaptic vesicle retrieval time is a cell-wide rather than individual-synapse property. Nat Neurosci 14:824–826.

Azarfar A, Calcini N, Huang C, Zeldenrust F, Celikel T (2018) Neural coding: A single neuron's perspective. Neurosci Biobehav Rev 94:238–247.

Babu LPA, Wang HY, Eguchi K, Guillaud L, Takahashi T (2020) Microtubule and actin differentially regulate synaptic vesicle cycling to maintain high-frequency neurotransmission. J Neurosci 40:131–142.

Bai Y, Xiang X, Liang C, Shi L (2015) Regulating Rac in the nervous system: Molecular function and disease implication of Rac GEFs and GAPs. Biomed Res Int 2015:632450.

Basu J, Betz A, Brose N, Rosenmund C (2007) Munc13-1 C1 domain activation lowers the energy barrier for synaptic vesicle fusion. J Neurosci 27:1200–1210.

Bleckert A, Photowala H, Alford S (2012) Dual pools of actin at presynaptic terminals. J Neurophysiol 107:3479–3492.

Bonnycastle K, Davenport EC, Cousin MA (2021) Presynaptic dysfunction in neurodevelopmental disorders: Insights from the synaptic vesicle life cycle. J Neurochem 157:179–207.

Borst JGG (2010) The low synaptic release probability in vivo. Trends Neurosci 33:259–266.

Borst JGG, Soria Van Hoeve J (2012) The calyx of held synapse: From model synapse to auditory relay. Annu Rev Physiol 74:199–224.

Bosco EE, Mulloy JC, Zheng Y (2009) Rac1 GTPase: A "Rac" of all trades. Cell Mol Life Sci 66:370–374.

Brette R (2015) Philosophy of the spike: Rate-based vs. Spike-based theories of the brain. Front Syst Neurosci 9:151.

Chanaday NL, Kavalali ET (2020) Is Ca2+ Essential for Synaptic Vesicle Endocytosis? Trends Neurosci 43:77–79.

Chen Z, Cooper B, Kalla S, Varoqueaux F, Young SM (2013) The munc13 proteins differentially regulate readily releasable pool dynamics and calcium-dependent recovery at a central synapse. J Neurosci 33:8336–8351.

Chen Z, Das B, Nakamura Y, DiGregorio DA, Young SM, Nakamura XY, DiGregorio DA, Young SM (2015) Ca2+ Channel to Synaptic Vesicle Distance Accounts for the Readily Releasable Pool Kinetics at a Functionally Mature Auditory Synapse. J Neurosci 35:2083–2100.

Cingolani LA, Goda Y (2008) Actin in action: The interplay between the actin cytoskeleton and synaptic efficacy. Nat Rev Neurosci 9:344–356.

Cole JC, Villa BRS, Wilkinson RS (2000) Disruption of actin impedes transmitter release in snake motor terminals. J Physiol 525 Pt 3:579–586.

Crins TTHH, Rusu SI, Rodríguez-Contreras A, Borst JGG (2011) Developmental changes in short-term plasticity at the rat calyx of Held synapse. J Neurosci 31:11706–11717.

Dietz DM et al. (2012) Rac1 is essential in cocaine-induced structural plasticity of nucleus accumbens neurons. Nat Neurosci 15:891–896.

Dong W, Radulovic T, Goral RO, Thomas C, Suarez Montesinos M, Guerrero-Given D, Hagiwara A, Putzke T, Hida Y, Abe M, Sakimura K, Kamasawa N, Ohtsuka T, Young SM (2018) CAST/ELKS Proteins Control Voltage-Gated Ca 2+ Channel Density and Synaptic Release Probability at a Mammalian Central Synapse. Cell Rep 24:284-293.e6.

Doussau F, Gasman S, Humeau Y, Vitiello F, Popoff M, Boquet P, Bader MF, Poulain B (2000) A Rho-related GTPase is involved in Ca2+-dependent neurotransmitter exocytosis. J Biol Chem 275:7764–7770.

Eggermann E, Bucurenciu I, Goswami SP, Jonas P (2012) Nanodomain coupling between Ca^{2+} channels and sensors of exocytosis at fast mammalian synapses. Nat Rev Neurosci 13:7–

21.
Eguchi K, Taoufiq Z, Thorn-Seshold O, Trauner D, Hasegawa M, Takahashi T (2017) Wild-Type Monomeric α-Synuclein Can Impair Vesicle Endocytosis and Synaptic Fidelity via Tubulin Polymerization at the Calyx of Held. J Neurosci 37:6043–6052.
Elmqvist D, Quastel DM (1965) A quantitative study of end-plate potentials in isolated human muscle. J Physiol 178:505–529.
Englitz B, Tolnai S, Typlt M, Jost J, Rübsamen R (2009) Reliability of synaptic transmission at the synapses of held in vivo under acoustic stimulation. PLoS One 4:e7014.
Fedchyshyn MJ, Wang L-Y (2007) Activity-dependent changes in temporal components of neurotransmission at the juvenile mouse calyx of Held synapse. J Physiol 581:581–602.
Fedchyshyn MJ, Wang LY (2005) Developmental transformation of the release modality at the calyx of held synapse. J Neurosci 25:4131–4140.
Forsberg M, Seth H, Björefeldt A, Lyckenvik T, Andersson M, Wasling P, Zetterberg H, Hanse E (2019) Ionized calcium in human cerebrospinal fluid and its influence on intrinsic and synaptic excitability of hippocampal pyramidal neurons in the rat. J Neurochem 149:452–470.
Forsythe ID, Barnes-Davies M (1993a) The binaural auditory pathway: excitatory amino acid receptors mediate dual timecourse excitatory postsynaptic currents in the rat medial nucleus of the trapezoid body. Proceedings Biol Sci 251:151–157.
Forsythe ID, Barnes-Davies M (1993b) The binaural auditory pathway: membrane currents limiting multiple action potential generation in the rat medial nucleus of the trapezoid body. Proceedings Biol Sci 251:143–150.
Friauf E, Fischer AU, Fuhr MF (2015) Synaptic plasticity in the auditory system: a review. Cell Tissue Res 361:177–213.
Gentile JE, Carrizales MG, Koleske AJ (2022) Control of Synapse Structure and Function by Actin and Its Regulators. Cells 11:603.
Ghanbari A, Ren N, Keine C, Stoelzel C, Englitz B, Swadlow HA, Stevenson IH (2020) Modeling the short-term dynamics of in vivo excitatory spike transmission. J Neurosci 40:4185–4202.
Glogauer M, Marchal CC, Zhu F, Worku A, Clausen BE, Foerster I, Marks P, Downey GP, Dinauer M, Kwiatkowski DJ (2003) Rac1 Deletion in Mouse Neutrophils Has Selective Effects on Neutrophil Functions. J Immunol 170:5652–5657.
Grothe B, Pecka M, McAlpine D (2010) Mechanisms of sound localization in mammals. Physiol Rev 90:983–1012.
Hallermann S, Silver RA (2013) Sustaining rapid vesicular release at active zones: Potential roles for vesicle tethering. Trends Neurosci 36:185–194.
Haustein MD, Reinert T, Warnatsch A, Englitz B, Dietz B, Robitzki A, R??bsamen R, Milenkovic I, Rübsamen R, Milenkovic I, R??bsamen R, Milenkovic I, Rübsamen R, Milenkovic I (2008) Synaptic transmission and short-term plasticity at the calyx of Held synapse revealed by multielectrode array recordings. J Neurosci Methods 174:227–236.
Hentschke H, Stüttgen MC (2011) Computation of measures of effect size for neuroscience data sets. Eur J Neurosci 34:1887–1894.
Hua Y, Woehler A, Kahms M, Haucke V, Neher E, Klingauf J (2013) Blocking endocytosis enhances short-term synaptic depression under conditions of normal availability of vesicles. Neuron 80:343–349.
Iwasaki S, Momiyama A, Uchitel OD, Takahashi T (2000) Developmental changes in calcium channel types mediating central synaptic transmission. J Neurosci 20:59–65.
Iwasaki S, Takahashi T (1998) Developmental changes in calcium channel types mediating synaptic transmission in rat auditory brainstem. J Physiol 509:419–423.
Iwasaki S, Takahashi T (2001) Developmental regulation of transmitter release at the calyx of Held in rat auditory brainstem. J Physiol 534:861–871.
Jensen TP, Filoteo AG, Knopfel T, Empson RM (2007) Presynaptic plasma membrane Ca2+ ATPase isoform 2a regulates excitatory synaptic transmission in rat hippocampal CA3. J

Physiol 579:85–99.
Johnston J, Forsythe ID, Kopp-Scheinpflug C (2010) Going native: Voltage-gated potassium channels controlling neuronal excitability. J Physiol 588:3187–3200.
Joris PX, Schreiner CE, Rees A (2004) Neural Processing of Amplitude-Modulated Sounds. Physiol Rev 84:541–577.
Joris PX, Trussell LO (2018) The Calyx of Held: A Hypothesis on the Need for Reliable Timing in an Intensity-Difference Encoder. Neuron 100:534–549.
Jung JH, Kirk LM, Bourne JN, Harris KM (2021) Shortened tethering filaments stabilize presynaptic vesicles in support of elevated release probability during LTP in rat hippocampus. Proc Natl Acad Sci U S A 118:1–8.
Kaeser PS, Regehr WG (2014) Molecular mechanisms for synchronous, asynchronous, and spontaneous neurotransmitter release. Annu Rev Physiol 76:333–363.
Kavalali ET (2014) The mechanisms and functions of spontaneous neurotransmitter release. Nat Rev Neurosci 16:5–16.
Kavalali ET (2020) Neuronal Ca2+ signalling at rest and during spontaneous neurotransmission. J Physiol 598:1649–1654.
Keine C, Rübsamen R, Englitz B (2016) Inhibition in the auditory brainstem enhances signal representation and regulates gain in complex acoustic environments. Elife 5:19295.
Klug A, Borst JGG, Carlson BA, Kopp-Scheinpflug C, Klyachko VA, Xu-Friedman MA (2012) How Do Short-Term Changes at Synapses Fine-Tune Information Processing? J Neurosci 32:14058–14063.
Kumanogoh H, Miyata S, Sokawa Y, Maekawa S (2001) Biochemical and morphological analysis on the localization of Rac1 in neurons. Neurosci Res 39:189–196.
Kusick GF, Chin M, Raychaudhuri S, Lippmann K, Adula KP, Hujber EJ, Vu T, Davis MW, Jorgensen EM, Watanabe S (2020) Synaptic vesicles transiently dock to refill release sites. Nat Neurosci 23:1329–1338.
Lee JS, Ho W-KK, Lee S-HH (2012) Actin-dependent rapid recruitment of reluctant synaptic vesicles into a fast-releasing vesicle pool. Proc Natl Acad Sci U S A 109:E765-74.
Lee JS, Ho W-KK, Neher E, Lee S-HH (2013) Superpriming of synaptic vesicles after their recruitment to the readily releasable pool. Proc Natl Acad Sci U S A 110:15079–15084.
Lidierth M (2009) sigTOOL: A MATLAB-based environment for sharing laboratory-developed software to analyze biological signals. J Neurosci Methods 178:188–196.
Lorteije JAMM, Borst JGG (2011) Contribution of the mouse calyx of Held synapse to tone adaptation. Eur J Neurosci 33:251–258.
Lorteije JAMM, Rusu SI, Kushmerick C, Borst JGG (2009) Reliability and precision of the mouse calyx of Held synapse. J Neurosci 29:13770–13784.
Lübbert M, Goral RO, Keine C, Thomas C, Guerrero-Given D, Putzke T, Satterfield R, Kamasawa N, Young SM (2019) CaV2.1 α1 Subunit Expression Regulates Presynaptic CaV2.1 Abundance and Synaptic Strength at a Central Synapse. Neuron 101:260-273.e6.
Lübbert M, Goral RO, Satterfield R, Putzke T, van den Maagdenberg AM, Kamasawa N, Young SM (2017) A novel region in the Ca V 2.1 α 1 subunit C-terminus regulates fast synaptic vesicle fusion and vesicle docking at the mammalian presynaptic active zone. Elife 6:1–22.
Mc Laughlin M, van der Heijden M, Joris PX (2008) How secure is in vivo synaptic transmission at the calyx of Held? J Neurosci 28:10206–10219.
Miki T, Malagon G, Pulido C, Llano I, Neher E, Marty A, Correspondence AM, Marty A (2016) Actin- and Myosin-Dependent Vesicle Loading of Presynaptic Docking Sites Prior to Exocytosis. Neuron 91:808–823.
Montesinos MS, Dong W, Goff K, Das B, Guerrero-Given D, Schmalzigaug R, Premont RT, Satterfield R, Kamasawa N, Young SM (2015) Presynaptic Deletion of GIT Proteins Results in Increased Synaptic Strength at a Mammalian Central Synapse. Neuron 88:918–925.
Montesinos MS, Satterfield R, Young SM (2016) Helper-Dependent Adenoviral Vectors and Their Use for Neuroscience Applications. In: High-Resolution Imaging of Cellular Proteins,

pp 73–90.
Morales M, Colicos MA, Goda Y (2000) Actin-Dependent Regulation of Neurotransmitter Release at Central Synapses. Neuron 27:539–550.
Neher E (2010) What is rate-limiting during sustained synaptic activity: Vesicle supply or the availability of release sites. Front Synaptic Neurosci 2:1–6.
Neher E (2015) Merits and Limitations of Vesicle Pool Models in View of Heterogeneous Populations of Synaptic Vesicles. Neuron 87:1131–1142.
Neher E, Brose N (2018) Dynamically Primed Synaptic Vesicle States: Key to Understand Synaptic Short-Term Plasticity. Neuron 100:1283–1291.
Neher E, Sakaba T (2008) Multiple Roles of Calcium Ions in the Regulation of Neurotransmitter Release. Neuron 59:861–872.
O'neil SD, Rácz B, Brown WE, Gao Y, Soderblom EJ, Yasuda R, Soderling SH (2021) Action potential-coupled rho gtpase signaling drives presynaptic plasticity. Elife 10:1–44.
Pulido C, Marty A (2017) Quantal fluctuations in central mammalian synapses: Functional role of vesicular docking sites. Physiol Rev 97:1403–1430.
Quastel DMJ (1997) The binomial model in fluctuation analysis of quantal neurotransmitter release. Biophys J 72:728–753.
Radulovic T, Dong W, Goral RO, Thomas CI, Veeraraghavan P, Montesinos MS, Guerrero-Given D, Goff K, Lübbert M, Kamasawa N, Ohtsuka T, Young SM (2020) Presynaptic development is controlled by the core active zone proteins CAST/ELKS. J Physiol 598:2431–2452.
Reijnders MRF et al. (2017) RAC1 Missense Mutations in Developmental Disorders with Diverse Phenotypes. Am J Hum Genet 101:466–477.
Reinagel P, Laughlin S (2001) Natural stimulus statistics. Network 12:237–240.
Richardson A, Ciampani V, Stancu M, Bondarenko K, Newton S, Steinert JR, Pilati N, Graham BP, Kopp-Scheinpflug C, Forsythe ID (2022) Kv3.3 subunits control presynaptic action potential waveform and neurotransmitter release at a central excitatory synapse. Elife 11:1–34.
Ritzau-Jost A, Jablonski L, Viotti J, Lipstein N, Eilers J, Hallermann S (2018) Apparent calcium dependence of vesicle recruitment. J Physiol 596:4693–4707.
Rollenhagen A, Lübke JHRR (2006) The morphology of excitatory central synapses: From structure to function. Cell Tissue Res 326:221–237.
Rothman JS, Silver RA (2018) Neuromatic: An integrated open-source software toolkit for acquisition, analysis and simulation of electrophysiological data. Front Neuroinform 12:1–21.
Rust MB, Maritzen T (2015) Relevance of presynaptic actin dynamics for synapse function and mouse behavior. Exp Cell Res 335:165–171.
Sakaba T (2006) Roles of the Fast-Releasing and the Slowly Releasing Vesicles in Synaptic Transmission at the Calyx of Held. J Neurosci 26:5863–5871.
Sakaba T, Neher E (2003) Involvement of actin polymerization in vesicle recruitment at the calyx of held synapse. J Neurosci 23:837–846.
Sätzler K, Söhl LF, Bollmann JH, Borst JGG, Frotscher M, Sakmann B, Lübke JHRR (2002) Three-dimensional reconstruction of a calyx of Held and its postsynaptic principal neuron in the medial nucleus of the trapezoid body. J Neurosci 22:10567–10579.
Scheuss V, Neher E (2001) Estimating synaptic parameters from mean, variance, and covariance in trains of synaptic responses. Biophys J 81:1970–1989.
Schindelin J, Arganda-Carreras I, Frise E, Kaynig V, Longair M, Pietzsch T, Preibisch S, Rueden C, Saalfeld S, Schmid B, Tinevez JY, White DJ, Hartenstein V, Eliceiri K, Tomancak P, Cardona A (2012) Fiji: An open-source platform for biological-image analysis. Nat Methods 9:676–682.
Schneggenburger R, Rosenmund C (2015) Molecular mechanisms governing Ca(2+) regulation of evoked and spontaneous release. Nat Neurosci 18:935–941.

Schotten S, Meijer M, Walter AM, Huson V, Mamer L, Kalogreades L, ter Veer M, Ruiter M, Brose N, Rosenmund C, Sørensen JB, Verhage M, Cornelisse LN (2015) Additive effects on the energy barrier for synaptic vesicle fusion cause supralinear effects on the vesicle fusion rate. Elife 4:1–25.

Shimshek DR, Kim J, Hübner MR, Spergel DJ, Buchholz F, Casanova E, Stewart AF, Seeburg PH, Sprengel R (2002) Codon-improved Cre recombinase (iCre) expression in the mouse. Genesis 32:19–26.

Sonntag M, Englitz B, Kopp-Scheinpflug C, Rübsamen R (2009) Early postnatal development of spontaneous and acoustically evoked discharge activity of principal cells of the medial nucleus of the trapezoid body: An in vivo study in mice. J Neurosci 29:9510–9520.

Sonntag M, Englitz B, Typlt M, Rübsamen R (2011) The calyx of Held Develops Adult-Like Dynamics And Reliability by Hearing Onset In The Mouse In vivo. J Neurosci 31:6699–6709.

Spirou GA, Brownell WE, Zidanic M (1990) Recordings from cat trapezoid body and HRP labeling of globular bushy cell axons. J Neurophysiol 63:1169–1190.

Tanaka M, Sakaba T, Miki T (2021) Quantal analysis estimates docking site occupancy determining short-term depression at hippocampal glutamatergic synapses. J Physiol 599:5301–5327.

Taschenberger H, Leão RM, Rowland KC, Spirou GA, von Gersdorff H (2002) Optimizing synaptic architecture and efficiency for high-frequency transmission. Neuron 36:1127–1143.

Thanawala MS, Regehr WG (2013) Presynaptic calcium influx controls neurotransmitter release in part by regulating the effective size of the readily releasable pool. J Neurosci 33:4625–4633.

Thanawala MS, Regehr WG (2016) Determining synaptic parameters using high-frequency activation. J Neurosci Methods 264:136–152.

Theunissen FE, Elie JE (2014) Neural processing of natural sounds. Nat Rev Neurosci 15:355–366.

Thomas CI, Keine C, Okayama S, Satterfield R, Musgrove M, Guerrero-Given D, Kamasawa N, Young SM (2019) Presynaptic Mitochondria Volume and Abundance Increase during Development of a High-Fidelity Synapse. J Neurosci 39:7994–8012.

Threadgill R, Bobb K, Ghosh A (1997) Regulation of dendritic growth and remodeling by Rho, Rac, and Cdc42. Neuron 19:625–634.

Tolnai S, Hernandez O, Englitz B, Rübsamen R, Malmierca MS (2008) The medial nucleus of the trapezoid body in rat: Spectral and temporal properties vary with anatomical location of the units. Eur J Neurosci 27:2587–2598.

Torres VI, Vallejo D, Inestrosa NC (2017) Emerging Synaptic Molecules as Candidates in the Etiology of Neurological Disorders. Neural Plast 2017.

Traynelis SF (1998) Software-based correction of single compartment series resistance errors. J Neurosci Methods 86:25–34.

Vere-Jones D (1966) Simple Stochastic Models for the Release of Quanta of Transmitter From a Nerve Terminal. Aust J Stat 8:53–63.

Waites CL, Garner CC (2011) Presynaptic function in health and disease. Trends Neurosci 34:326–337.

Waites CL, Leal-Ortiz S a., Andlauer TFMM, Sigrist SJ, Garner CC (2011) Piccolo regulates the dynamic assembly of presynaptic F-actin. J Neurosci 31:14250–14263.

Wang LY, Gan L, Forsythe ID, Kaczmarek LK (1998) Contribution of the Kv3.1 potassium channel to high frequency firing in mouse auditory neurones. J Physiol 509:183–194.

Wang LY, Kaczmarek LK (1998) High-frequency firing helps replenish the readily releasable pool of synaptic vesicles. Nature 394:384–388.

Watanabe S, Liu Q, Davis MW, Hollopeter G, Thomas N, Jorgensen NB, Jorgensen EM (2013a) Ultrafast endocytosis at Caenorhabditis elegans neuromuscular junctions. Elife 2013:1–24.

Watanabe S, Rost BR, Camacho-Pérez M, Davis MW, Söhl-Kielczynski B, Rosenmund C, Jorgensen EM (2013b) Ultrafast endocytosis at mouse hippocampal synapses. Nature 504:242–247.

Wimmer VC, Horstmann H, Groh A, Kuner T (2006) Donut-like topology of synaptic vesicles with a central cluster of mitochondria wrapped into membrane protrusions: A novel structure-function module of the adult calyx of held. J Neurosci 26:109–116.

Wondolowski J, Dickman D (2013) Emerging links between homeostatic synaptic plasticity and neurological disease. Front Cell Neurosci 7:223.

Wright WJ, Graziane NM, Neumann PA, Hamilton PJ, Cates HM, Fuerst L, Spenceley A, MacKinnon-Booth N, Iyer K, Huang YH, Shaham Y, Schlüter OM, Nestler EJ, Dong Y (2020) Silent synapses dictate cocaine memory destabilization and reconsolidation. Nat Neurosci 23:32–46.

Wu L-GG, Chan CY (2022) Multiple Roles of Actin in Exo- and Endocytosis. Front Synaptic Neurosci 14:1–13.

Xu Z, Chen Y (2019) Spatiotemporal regulation of rho gtpases in neuronal migration. Cells 8.

Xue M, Craig TK, Xu J, Chao HT, Rizo J, Rosenmund C (2010) Binding of the complexin N terminus to the SNARE complex potentiates synaptic-vesicle fusogenicity. Nat Struct Mol Biol 17:568–575.

Yang H, Xu-Friedman MA (2015) Skipped-stimulus approach reveals that short-term plasticity dominates synaptic strength during ongoing activity. J Neurosci 35:8297–8307.

Yang Y-MM, Fedchyshyn MJ, Grande G, Aitoubah J, Tsang CW, Xie H, Ackerley CA, Trimble WS, Wang L-YY (2010) Septins regulate developmental switching from microdomain to nanodomain coupling of Ca2+ influx to neurotransmitter release at a central synapse. Neuron 67:100–115.

Yasuda R (2017) Biophysics of Biochemical Signaling in Dendritic Spines: Implications in Synaptic Plasticity. Biophys J 113:2152–2159.

Young SM, Neher E (2009) Synaptotagmin Has an Essential Function in Synaptic Vesicle Positioning for Synchronous Release in Addition to Its Role as a Calcium Sensor. Neuron 63:482–496.

Zamboni V, Jones R, Umbach A, Ammoni A, Passafaro M, Hirsch E, Merlo GR (2018) Rho GTPases in intellectual disability: From genetics to therapeutic opportunities. Int J Mol Sci 19:187–191.

Zhang H, Ben Zablah Y, Zhang H, Jia Z (2021) Rho Signaling in Synaptic Plasticity, Memory, and Brain Disorders. Front Cell Dev Biol 9:729076.

Zucker RS, Regehr WG (2002) Short-term synaptic plasticity. Annu Rev Physiol 64:355–405.

Figures legends

Fig. 1: Loss of presynaptic Rac1 after hearing onset does not affect calyx of Held gross morphology or ultrastructure. (**A**) Cre recombinase-expressing HdAds were injected into the cochlear nucleus of *Rac1*$^{fl/fl}$ mice at P14, yielding *Rac1*$^{-/-}$ calyces of Held. All experiments were performed at around four weeks of age. Cre-recombinase-expressing calyces could be visually identified by simultaneous expression of EGFP. (**B1**) Representative reconstruction of calyx terminals of *Rac1*$^{+/+}$ (left) and *Rac1*$^{-/-}$ (right) animals. (**B2**) Calyx morphology assessed by surface area (left) and volume (right) was not affected by the loss of Rac1 (**C1**) Representative EM images of the active zone (yellow) and docked SV (blue) to assess synaptic ultrastructure. (**C2**) SV distribution as a function of distance to AZ was not different between *Rac1*$^{+/+}$ and *Rac1*$^{-/-}$. (**C3**) AZ length and number of docked SV were comparable between *Rac1*$^{+/+}$ *and Rac1*$^{-/-}$*.* Box plot whiskers extend to the minimum/maximum within the 1.5 interquartile range; open markers indicate individual data points. For EM data, the results of three independent investigators were averaged. All data shown in the figure and the detailed results of statistical tests can be found in the supplementary files.

Fig. 2: Presynaptic Rac1 regulates synaptic vesicles release probability and synaptic strength. (**A**) Synaptic transmission at the calyx of Held – MNTB synapse was studied at P28 after deletion of Rac1 at P14 at different stimulation frequencies. (**A1, B1**) Representative evoked EPSCs for *Rac1*$^{+/+}$ (black) and *Rac1*$^{-/-}$(orange) at 50 Hz and 500 Hz stimulation frequency and (**C1**) Magnification of the first EPSC. Ablation of presynaptic Rac1 resulted in increased EPSC amplitude with no change in EPSC dynamics (**A2-A4**) At 50 Hz stimulation frequency, *Rac1*$^{-/-}$ showed stronger short-term depression and larger steady-state EPSC amplitudes. (**B2-B4**) At 500 Hz stimulation frequency, loss of Rac1 resulted in a lack of short-term facilitation and increased synaptic depression with no change in steady-state EPSC amplitude (**D1**) Population data showing an increase in first EPSC amplitude in *Rac1*$^{-/-}$ with little or no change in RRP size (**D2**) Population data for initial (left) and steady-state release

probability (right) indicating that release probability in *Rac1*$^{-/-}$ was elevated independent of estimation method and stimulation frequency. (**D3**) Population data of steady-state EPSC amplitudes and replenishment rates at 50 and 500 Hz stimulation frequency. *Rac1*$^{-/-}$ had larger steady-state EPSCs and faster replenishment at 50 Hz but not 500 Hz stimulation frequency. All data shown in the figure and the detailed results of statistical tests can be found in the supplementary files.

Fig. 3: Presynaptic loss of Rac1 increase calcium-independent neurotransmitter release. (**A**) Representative recordings of mEPSCs for *Rac1*$^{+/+}$ (left, black) and *Rac1*$^{-/-}$ (right, orange). (**B1-B4**) Rac1 deletion increased mEPSC frequency but did not affect mEPSC amplitude, rise time, or full width at half-maximal amplitude (FWHM). (**C**) The increased mEPSC rates at *Rac1*$^{-/-}$ were independent of presynaptic voltage-gated calcium channels (VGCC) as blocking VGCC with cadmium (Cd^{2+}) did not affect mEPSC frequency. All data shown in the figure and the detailed results of statistical tests can be found in the supplementary files.

Fig. 4: Presynaptic loss of Rac1 decreases SV synchronicity and prolongs EPSC onset at high-frequency stimulation. (**A**) Experiments were performed at low (50 Hz, A1) and high (500 Hz, A2) stimulation frequencies. Representative recordings of first ($EPSC_1$) and last ($EPSC_{50}$) EPSC in the stimulus train. Traces are aligned at the EPSC onset of the first EPSC. Stimulus artifacts are partially blanked for better visibility. Note the shift in the onset of $EPSC_{50}$ in *Rac1*$^{-/-}$ at 500 Hz but not 50 Hz (**B1**) Absolute EPSC onset delay for 50 Hz (gray and light orange) and 500 Hz (black and orange) stimulation. (**B2**) EPSC onset delay relative to $EPSC_1$ for 50 Hz (gray and light orange) and 500 Hz (black and orange). At 50 Hz, the EPSC onset delay was similar between *Rac1*$^{+/+}$ and *Rac1*$^{-/-}$. At 500 Hz, the EPSC onset delay was substantially larger at *Rac1*$^{-/-}$. For better visualization, only every second data point is shown. (**B3**) EPSC onset delay of the last ten EPSCs relative to $EPSC_1$ for 50 Hz and 500 Hz stimulation. EPSC delay of the last ten EPSC was not different between *Rac1*$^{+/+}$ and *Rac1*$^{-/-}$ at

50 Hz but increased for *Rac1*$^{-/-}$ at 500 Hz stimulation frequency. (**C1**) Analysis of EPSC synchronicity during 50 Hz and 500 Hz stimulation. Synchronicity was calculated by dividing the EPSC amplitudes by the EPSC charge. Note the more severe loss of EPSC synchronicity for *Rac1*$^{-/-}$ at 500 Hz stimulation. For better visualization only every second data point is shown (**C2**) EPSC synchronicity was not different for $EPSC_1$, but slightly reduced for *Rac1*$^{-/-}$ at 50 Hz and substantially lower at 500 Hz stimulation frequency. (**C3**) EPSC synchronicity of last ten EPSCs normalized to $EPSC_1$. Note the progressive loss of synchronicity in *Rac1*$^{-/-}$ with increasing stimulation frequency. All data shown in the figure and the detailed results of statistical tests can be found in the supplementary files.

Fig. 5: Loss of presynaptic Rac1 facilitates synaptic vesicle recovery. (**A**) Recovery of single EPSC and RRP recovery was measured by two consecutive train stimuli (depleting stimulus and recovery stimulus) at 500 Hz at varying recovery intervals. (**A**) Single EPSC recovery. (**A1**) Representative traces for *Rac1*$^{+/+}$ (black) and *Rac1*$^{-/-}$ (orange) for recovery intervals ranging from 20 ms to 16 s. (**A2**) Recovery of absolute EPSC amplitudes as a function of recovery interval with magnification of short intervals (right). (**A3**) Fractional EPSC recovery as a function of recovery interval. (**B**) Recovery of the RRP (**B1**) Representative recovery traces after 100 ms and 2 s, the depleting stimulus train is the same as in A1. (**B2**) Fractional RRP recovery was faster in *Rac1*$^{-/-}$ compared to *Rac1*$^{+/+}$. (**B3**) Recovery of the paired-pulse ratio (PPR) of the first two EPSCs of the recovery train. PPR was consistently lower in *Rac1*$^{-/-}$ but the difference was emphasized at longer recovery intervals. All data shown in the figure and the detailed results of statistical tests can be found in the supplementary files.

Fig. 6: Alterations in presynaptic release probability did not impair the reliability of action potential generation during *in vivo*-like activity. (**A1**) AP firing was recorded in response to *in vivo*-like stimulation patterns derived from responses to sinusoidal amplitude-modulated sounds at different modulation frequencies. Raster plot shows three representative stimulation patterns

(**A2**) Representative traces of loose-patch recordings during afferent fiber stimulation with in vivo-like activity for *Rac1*$^{+/+}$ (black) and *Rac1*$^{-/-}$ (orange). (**B1**) Fraction of successful AP generation was not different between *Rac1*$^{+/+}$ and *Rac1*$^{-/-}$ independent of modulation frequency (**B2**) AP jitter defined as the standard deviation of AP latencies was not changed in *Rac1*$^{-/-}$ neither for the complete stimulus nor as a function of stimulus modulation frequency. (**C1**) AP jitter and AP delay as a function of preceding inter-spike interval (**C2**) AP jitter and AP delay as a function of preceding activity level. Note the increased AP jitter and AP delay in *Rac1*$^{-/-}$ at higher activity levels. All data shown in the figure and the detailed results of statistical tests can be found in the supplementary files.

Fig. 7: Proposed model of Rac1's presynaptic role in regulating synaptic transmission. In the proposed model loss of Rac1 results in changes in F-actin at the active zone, thereby reducing the barrier function between SVs and the plasma membrane. The resulting increase in SV fusogenicity increases Pr and synaptic strength.

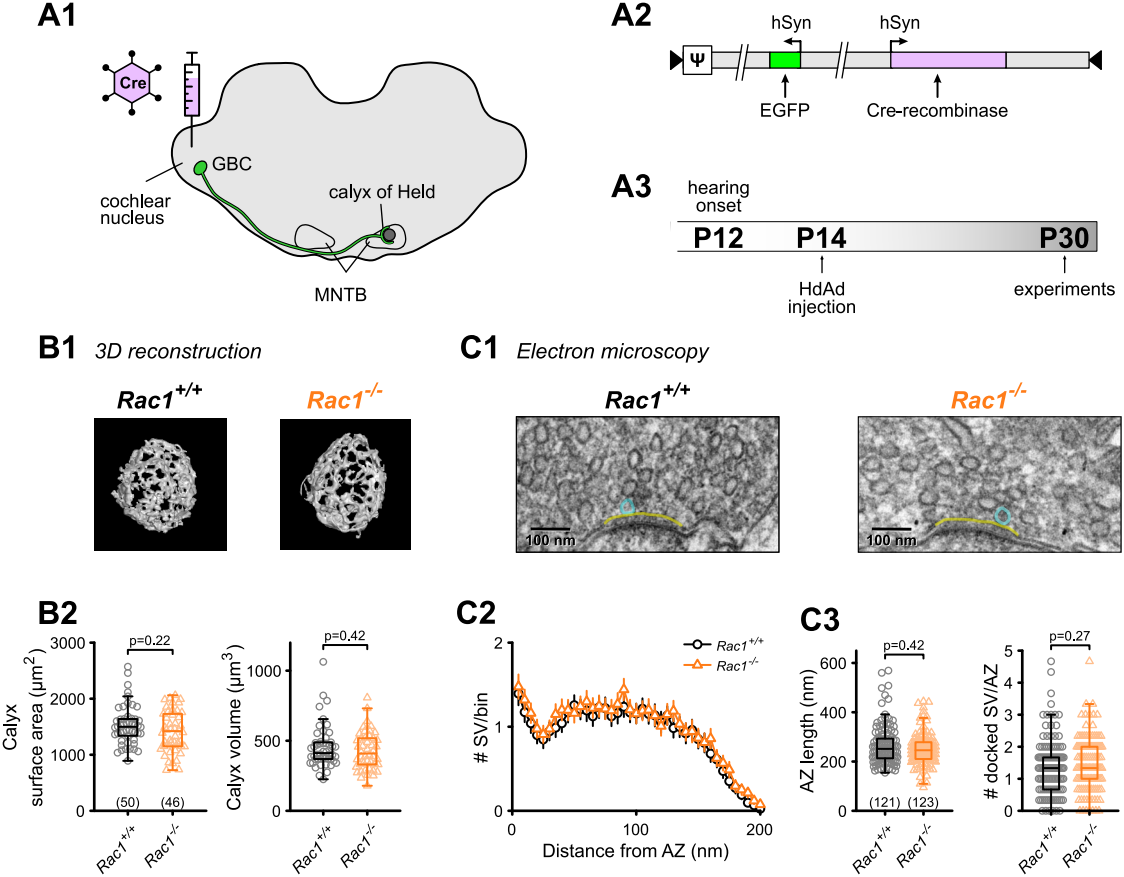
A1
Cre
GBC
cochlear nucleus
calyx of Held
MNTB
A2
hSyn
hSyn
Ψ
EGFP
Cre-recombinase
A3
hearing onset
P12
P14
P30
HdAd injection
experiments
B1
3D reconstruction
Rac1+/+
Rac1-/-
C1
Electron microscopy
Rac1+/+
Rac1-/-
100 nm
100 nm
B2
Calyx surface area (µm2)
p=0.22
(50)
(46)
Calyx volume (µm3)
p=0.42
Rac1+/+
Rac1-/-
C2
SV/bin
Rac1+/+
Rac1-/-
Distance from AZ (nm)
C3
AZ length (nm)
p=0.42
(121)
(123)
# docked SV/AZ
p=0.27
Rac1+/+
Rac1-/-

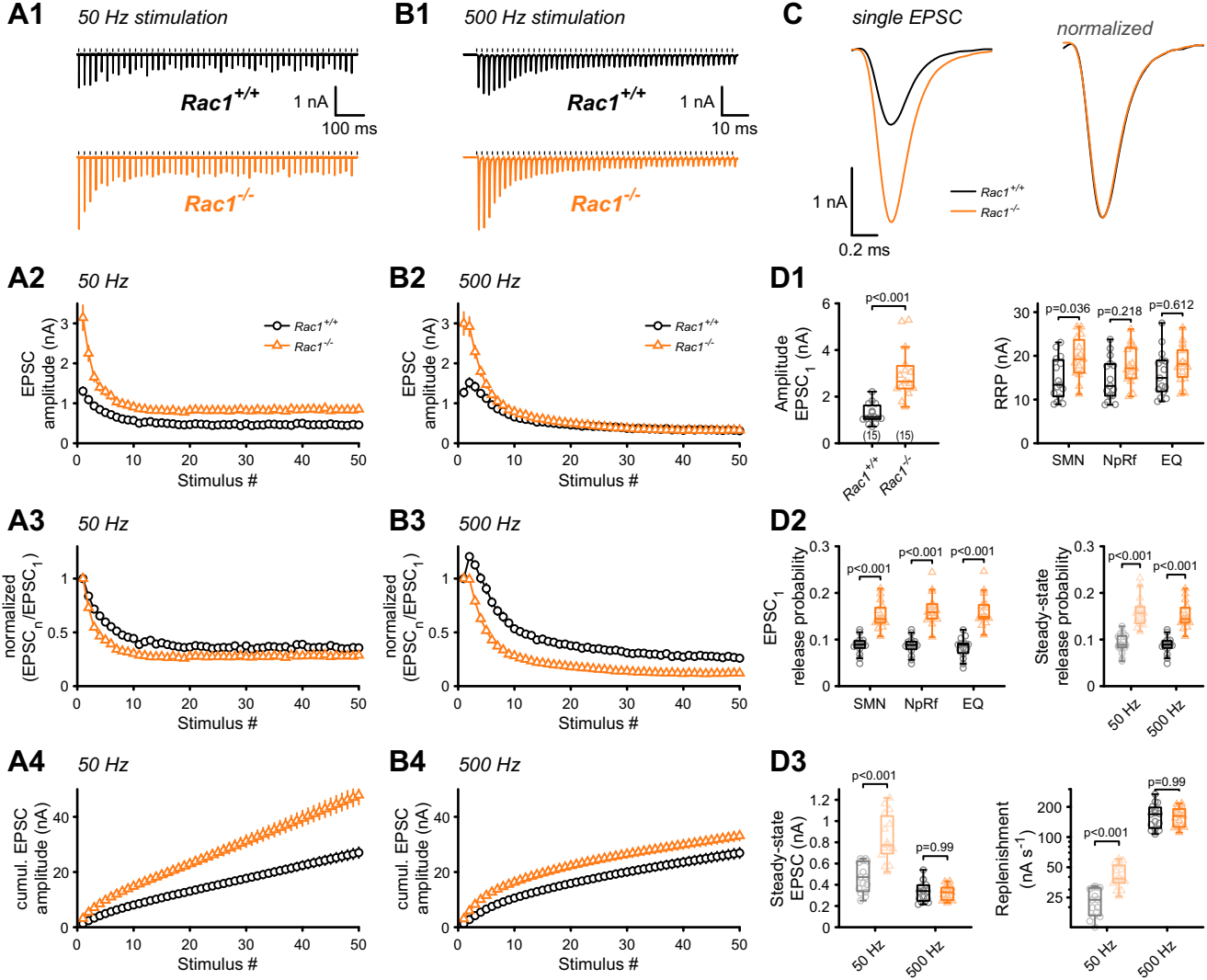
A1
50 Hz stimulation
Rac1+/+
1 nA
100 ms
Rac1-/-
B1
500 Hz stimulation
Rac1+/+
1 nA
10 ms
Rac1-/-
C
single EPSC
normalized
1 nA
0.2 ms
Rac1+/+
Rac1-/-
A2
50 Hz
EPSC amplitude (nA)
Stimulus #
B2
500 Hz
D1
Amplitude EPSC1 (nA)
p<0.001
(15)
(15)
RRP (nA)
p=0.036
p=0.218
p=0.612
SMN
NpRf
EQ
A3
50 Hz
normalized (EPSCn/EPSC1)
B3
500 Hz
D2
EPSC1 release probability
p<0.001
Steady-state release probability
50 Hz
500 Hz
A4
50 Hz
cumul. EPSC amplitude (nA)
B4
500 Hz
D3
Steady-state EPSC (nA)
p=0.99
Replenishment (nA s-1)

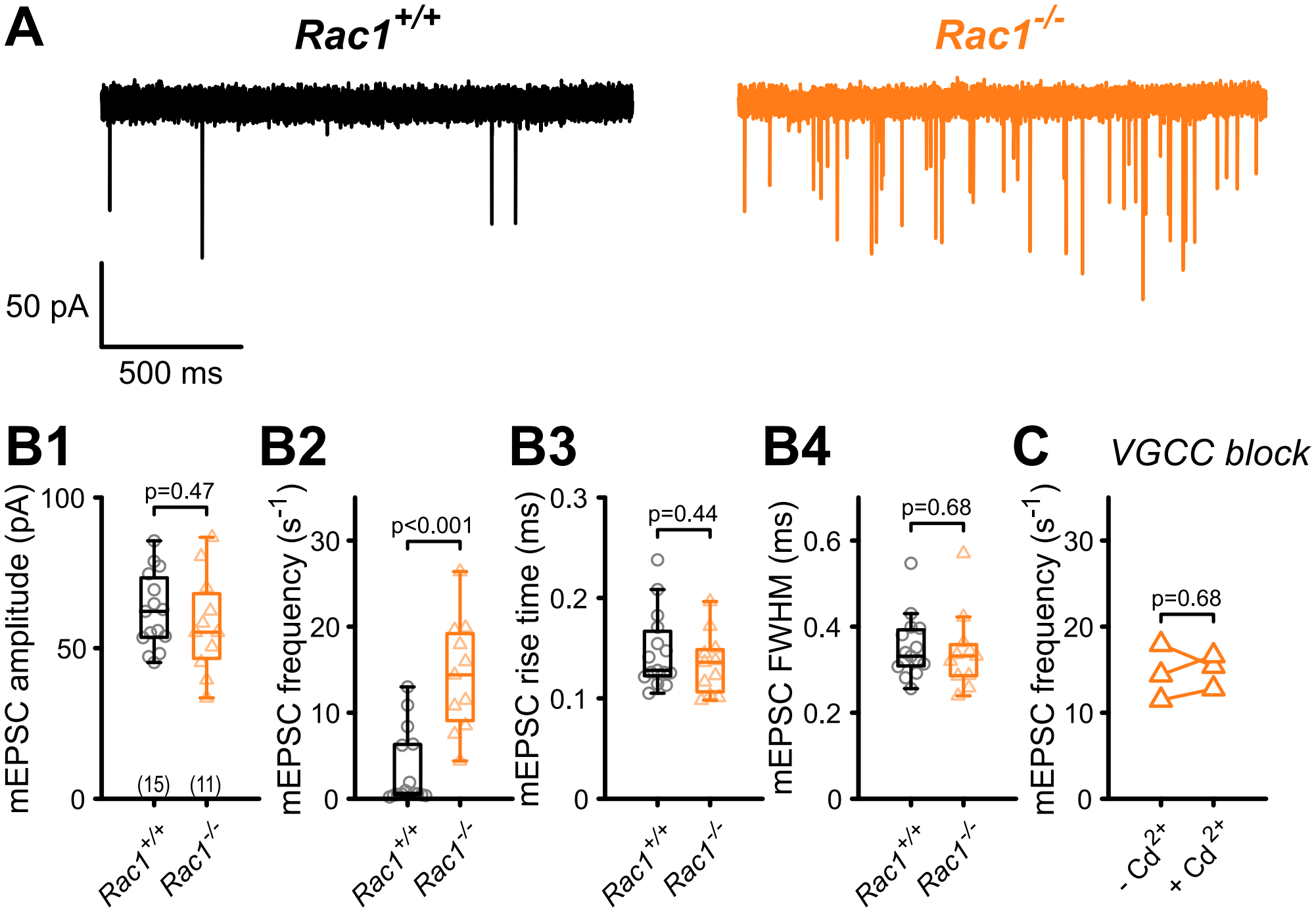
A
Rac1+/+
Rac1-/-
50 pA
500 ms
B1
B2
B3
B4
C
VGCC block
mEPSC amplitude (pA)
mEPSC frequency (s-1)
mEPSC rise time (ms)
mEPSC FWHM (ms)
p=0.47
p<0.001
p=0.44
p=0.68
p=0.68
(15)
(11)
Rac1+/+
Rac1-/-
- Cd2+
+ Cd2+

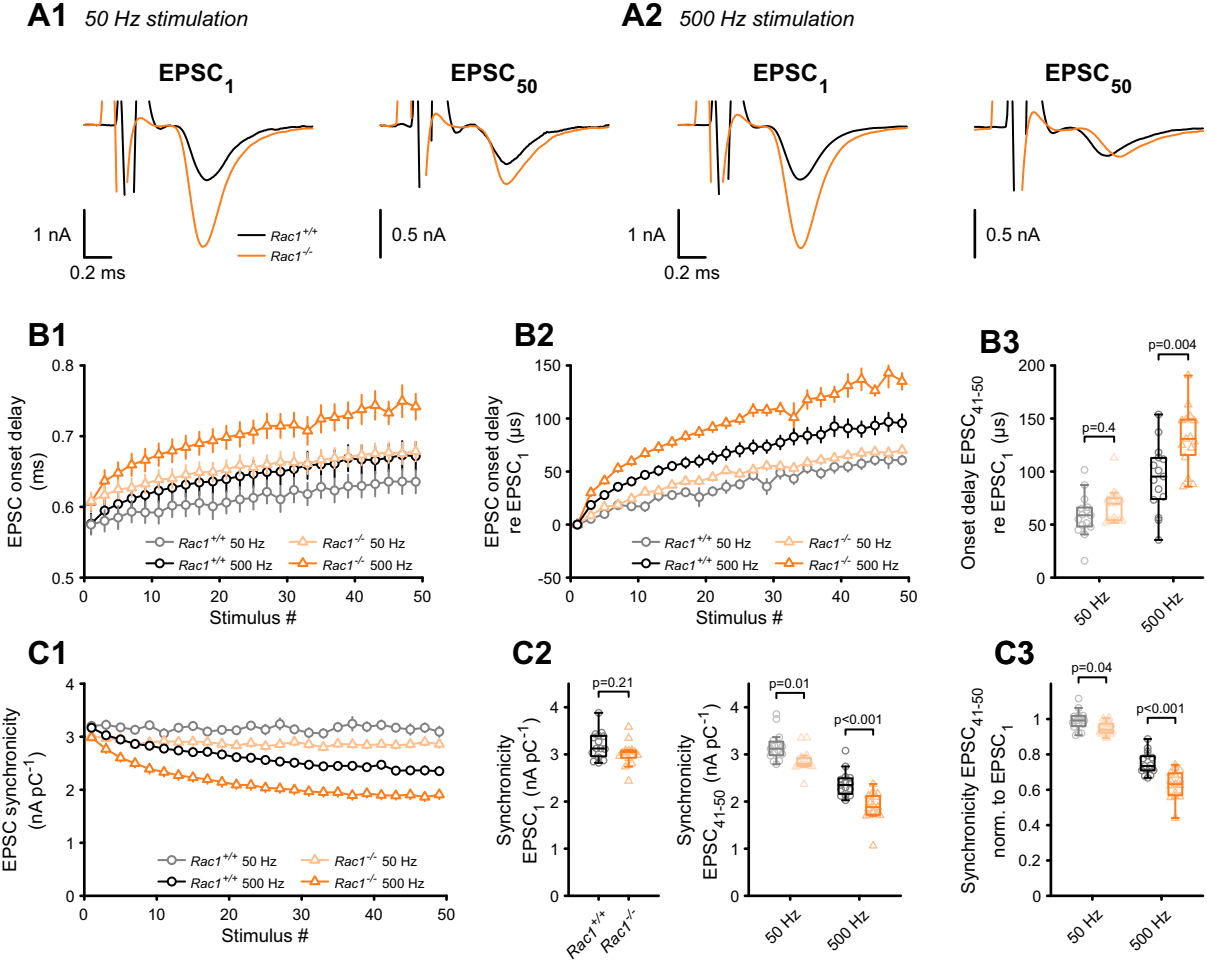
A1 50 Hz stimulation
A2 500 Hz stimulation
EPSC1
EPSC50
EPSC1
EPSC50
1 nA
0.2 ms
Rac1+/+
Rac1-/-
0.5 nA
1 nA
0.2 ms
0.5 nA
B1
EPSC onset delay (ms)
Stimulus #
Rac1+/+ 50 Hz
Rac1+/+ 500 Hz
Rac1-/- 50 Hz
Rac1-/- 500 Hz
B2
EPSC onset delay re EPSC1 (µs)
Stimulus #
B3
Onset delay EPSC41-50 re EPSC1 (µs)
p=0.4
p=0.004
50 Hz
500 Hz
C1
EPSC synchronicity (nA pC-1)
Stimulus #
C2
Synchronicity EPSC1 (nA pC-1)
p=0.21
Rac1+/+
Rac1-/-
Synchronicity EPSC41-50 (nA pC-1)
p=0.01
p<0.001
50 Hz
500 Hz
C3
Synchronicity EPSC41-50 norm. to EPSC1
p=0.04
p<0.001
50 Hz
500 Hz

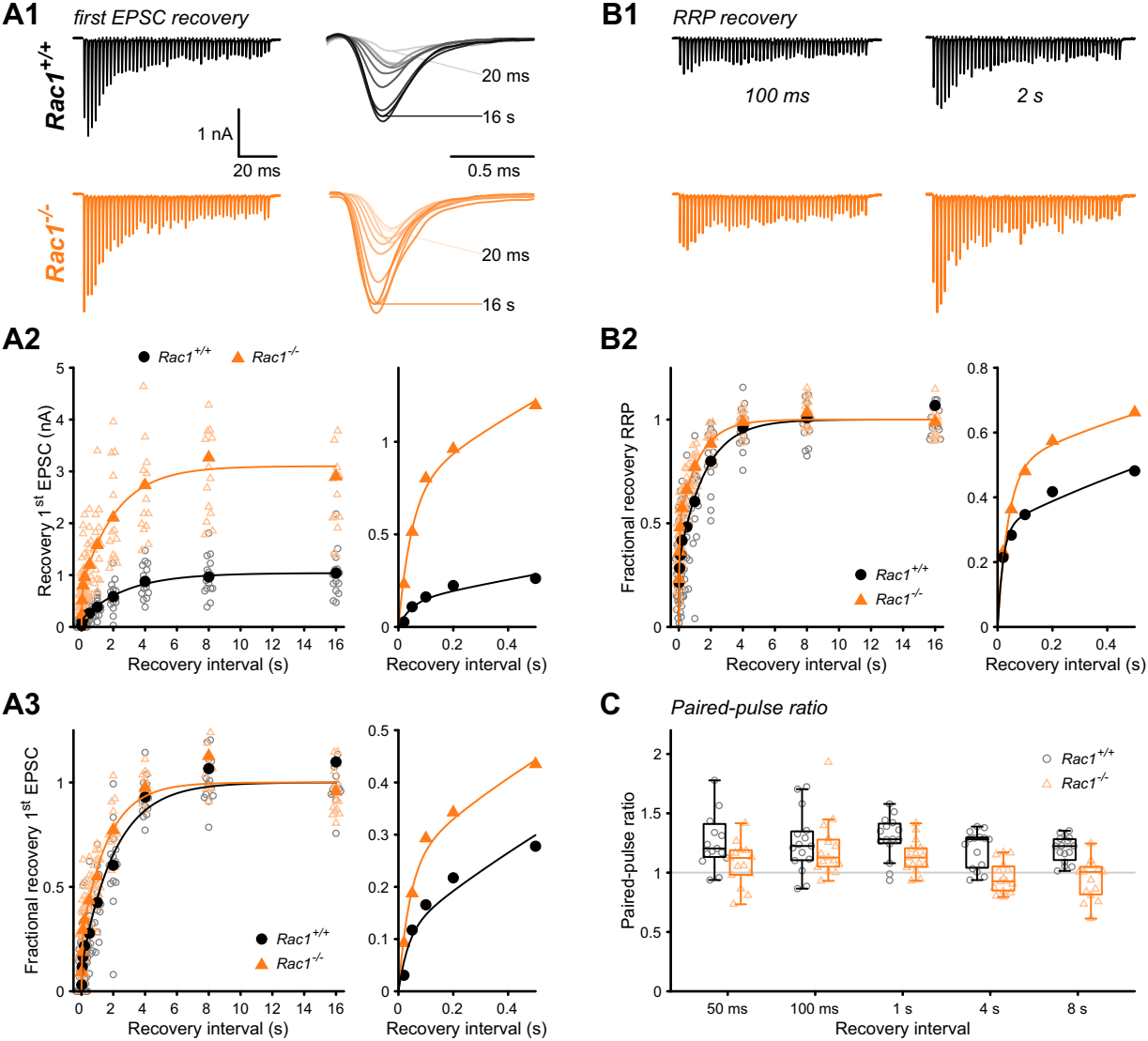
A1
first EPSC recovery
Rac1+/+
1 nA
20 ms
20 ms
16 s
0.5 ms
Rac1-/-
20 ms
16 s
B1
RRP recovery
100 ms
2 s
A2
Rac1+/+
Rac1-/-
Recovery 1st EPSC (nA)
Recovery interval (s)
Recovery interval (s)
B2
Fractional recovery RRP
Rac1+/+
Rac1-/-
Recovery interval (s)
Recovery interval (s)
A3
Fractional recovery 1st EPSC
Rac1+/+
Rac1-/-
Recovery interval (s)
Recovery interval (s)
C
Paired-pulse ratio
Rac1+/+
Rac1-/-
Paired-pulse ratio
50 ms
100 ms
1 s
4 s
8 s
Recovery interval

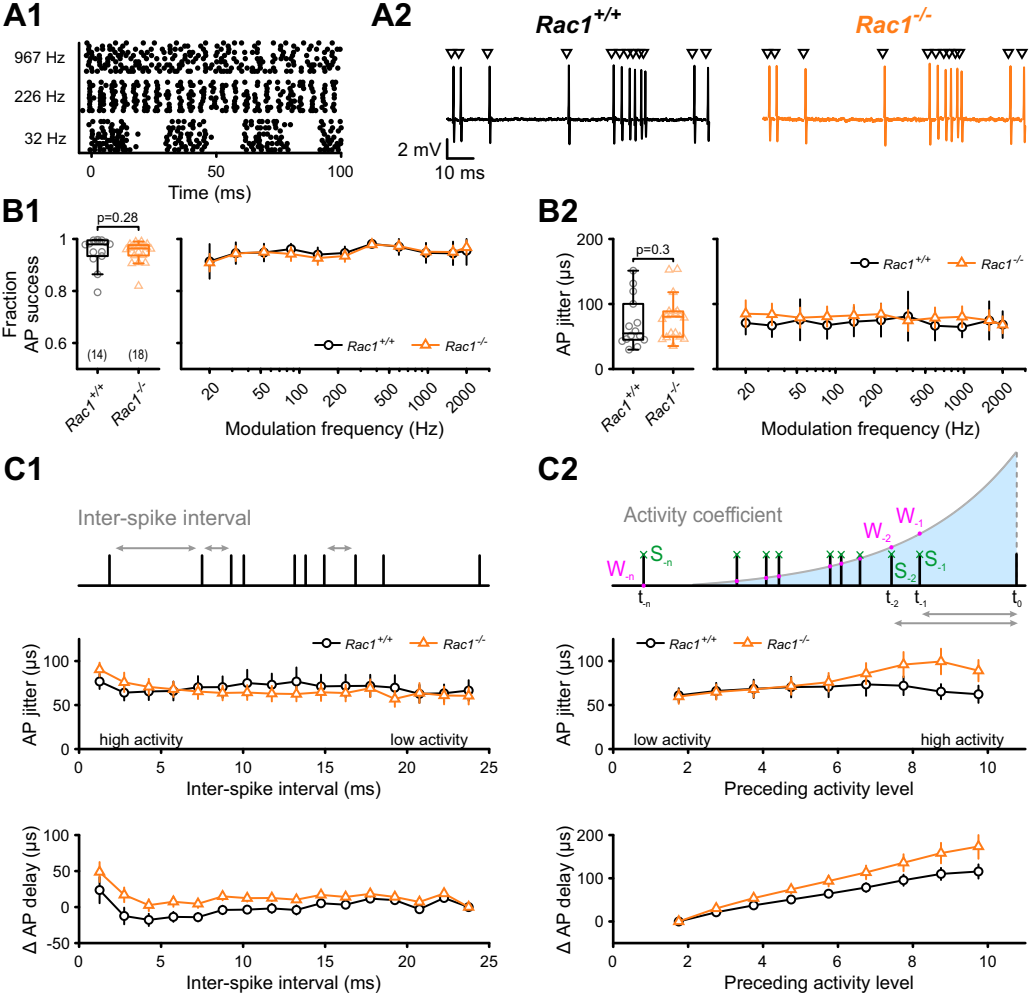
A1
967 Hz
226 Hz
32 Hz
0
50
100
Time (ms)
A2
Rac1+/+
Rac1-/-
2 mV
10 ms
B1
p=0.28
Fraction AP success
1
0.8
0.6
(14)
(18)
Rac1+/+
Rac1-/-
20
50
100
200
500
1000
2000
Modulation frequency (Hz)
B2
p=0.3
AP jitter (µs)
200
100
0
Rac1+/+
Rac1-/-
20
50
100
200
500
1000
2000
Modulation frequency (Hz)
C1
Inter-spike interval
AP jitter (µs)
100
50
0
high activity
low activity
0
5
10
15
20
25
Inter-spike interval (ms)
Δ AP delay (µs)
100
50
0
-50
0
5
10
15
20
25
Inter-spike interval (ms)
C2
Activity coefficient
W-n
S-n
W-2
W-1
S-2
S-1
t-n
t-2
t-1
t0
AP jitter (µs)
100
50
0
low activity
high activity
0
2
4
6
8
10
Preceding activity level
Δ AP delay (µs)
200
100
0
0
2
4
6
8
10
Preceding activity level

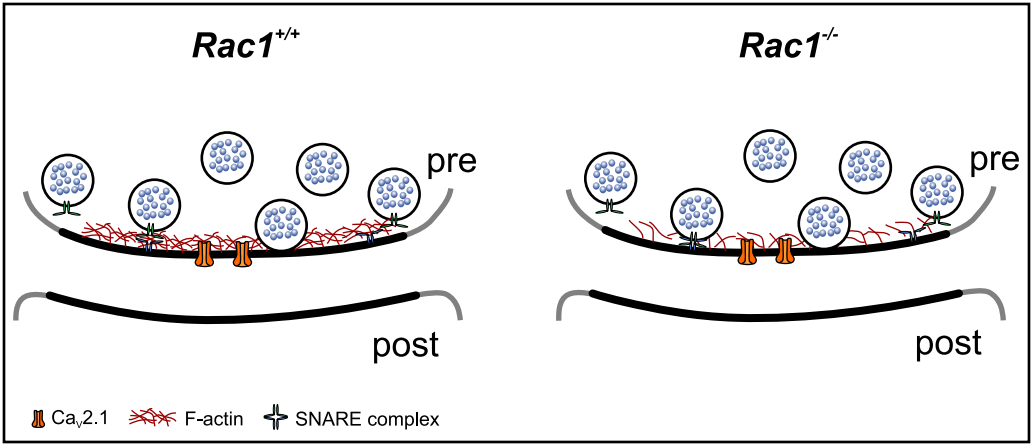
Rac1+/+
Rac1-/-
pre
post
pre
post
Cav2.1
F-actin
SNARE complex